Engineering Fracture Mechanics 295 (2024) 109720

Contents lists available at ScienceDirect

Engineering Fracture Mechanics

journal homepage: www.elsevier.com/locate/engfracmech

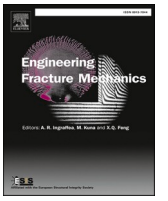

Fracture mechanics-based analysis of the fatigue limit of Ti6Al4V alloy specimens manufactured by SLM in as-built surface conditions by means of areal measurements

D. Rigon, F. Coppola, G. Meneghetti *

Department of Industrial Engineering, University of Padova, Via Venezia 1, 35131 Padova, Italy

ARTICLE INFO

Keywords:
Fatigue Thresholds
Fatigue Limit
Roughness
Areal Parameter
Linear Elastic Fracture Mechanics
Ti6Al4V
L-PBF
Additive Manufacturing

ABSTRACT

The fatigue limit of additively manufactured Ti6Al4V alloy specimens in as-built surface conditions is estimated using a fracture mechanics analysis involving different definitions of an effective crack size related to the areal parameter, S_v, of the surface texture, on which the fatigue limit is made to depend. The approach adopts the Extreme Value Statistics (EVS) to determine the largest S_v of the individual as well as the entire batch of specimens and is validated by comparison with the experimental results. Finally, the applicability of the approach by using the 1D roughness profile parameter, R_v, is discussed using the EVS with appropriate hypotheses.

1. Introduction

The development of fatigue design criteria for metallic components produced by means of additive manufacturing (AM) processes is experiencing a growing interest in several industrial sectors such as aerospace, automotive and biomedical. The main reason is due to a certain lack of knowledge on a reliable qualification of the structural durability of components produced by means of processes like Laser Powder Bed Fusion (L-PBF) and Direct Energy Deposition (DED), which operate on a layer-by-layer manufacturing principle [1–4].

The fatigue behaviour of metallic parts produced by AM basically suffers from two main process-inherent factors. The first is the presence of defects, which are mainly distributed in the surface substrate of the part, while the second is the rough as-built surface finish. The interaction between these factors plays a fundamental role for assessing the fatigue strength of AM components [5–14]. When the first factor is predominant, for example when parts are post-machined, it has been widely observed that the largest surface or subsurface defect governs the fatigue strength and fracture mechanics approaches proved suitable [15–22], such as those proposed by El Haddad Smith Topper (EHST) [23,24] or Murakami [25]. However, post-machining processes are often avoided to benefit from additively manufacturing components with very complex shapes. Therefore, considerable scientific effort has been focused on understanding the influence of the peculiar surface texture of as-built specimens on the fatigue behaviour. The standardised surface roughness parameters reported by ISO 4287:1997 [26], or the areal parameters proposed in ISO 25178 [27] are commonly used in several fatigue lifetime estimating methods. In this context, Greitemeier et al. proposed to estimate the S-N curve of as-built Ti6Al4V specimens produced both by direct metal laser sintering (DMLS) and electron beam melting (EBM) by integrating the NASGRO crack

* Corresponding author at: Department of Industrial Engineering, University of Padova, Via Venezia 1, 35131 Padova, Italy.
E-mail address: giovanni.meneghetti@unipd.it (G. Meneghetti).

https://doi.org/10.1016/j.engfracmech.2023.109720
Received 22 February 2023; Received in revised form 25 October 2023; Accepted 3 November 2023
Available online 15 November 2023

Nomenclature

a	crack length
a_0	El-Haddad-Smith-Topper material length parameter
a_{eff}	effective defect/crack size ($a_{eff} = \alpha^2\sqrt{area}$ or $a_{eff} = \alpha^2 a$)
A_0	control area where S_v is extracted
A_{ref}	reference area (in this study it is the entire surface of the gauge part of the specimen)
$f_{A_0}(S_v)$	probability density function of $F_{A_0}(S_v)$
$F_{A_0}(S_v)$	LEVD or Gumbel distribution of S_v, measured by adopting block maxima sampling with control areas A_0
$f_{A_{ref}}(S_v)$	probability density function of $F_{A_{ref}}(S_v)$
$F_{A_{ref}}(S_v)$	LEVD or Gumbel distribution of S_v, referred to A_{ref}
K_I	mode I stress intensity factor
L	microstructural length parameter
L_0	sampling length of a 1D roughness profile
R	load ratio ($R = \sigma_{min}/\sigma_{max}$)
R_{Sm}	mean spacing of a profile element widths (ISO 4287:1997) of a 1D roughness profile
R_v	largest profile valley depth (ISO 4287:1997) of a 1D roughness profile within L_0
$R_{v,max}$	largest R_v value within A_{ref} estimated by means of the EVS
S_v	maximum pit depth parameter (ISO 25178–2) of a 2D areal domain within A_0
$S_{v,max}$	largest S_v value within A_{ref} estimated by means of the EVS
s	standard deviation
T	return period
T_σ	stress scatter index
A	shape factor to evaluate the Stress Intensity Factor (SIF)
μ	mean value of a distribution
$\Delta\sigma_0$	defect-free fatigue limit in terms of nominal stress range (maximum value minus minimum value) for a fixed load ratio
$\Delta\sigma_g$	range of σ_g (maximum value minus minimum value)
$\Delta\sigma_{g,th}$	threshold range of σ_g
$\Delta K_{th,LC}$	threshold SIF range of long cracks for a given load ratio R.
σ_g	gross nominal stress acting on the gauge cross-section of the specimen
$\sigma_{y,0.2}$	0.2% yield stress
σ_{UTS}	ultimate tensile strength
$\sqrt{area}$	square root of the area of a defect projected onto the plane perpendicular to the maximum principal stress
$\sqrt{area}_R$	representative defect size related to a periodic array of cracks

Acronyms

ALM	Atzori Lazzarin Meneghetti model
AM	Additive Manufacturing
CT	Computed Tomography
EHST	El Haddad Smith Topper model
EVS	Extreme Value Statistics
LEVD	Largest Extreme Value Distribution
L-PBF	Laser-based Powder Bed Fusion
M	Murakami model
PS	Survival probability
SLM	Selective Laser Melting
SIF	Stress Intensity Factor

growth equation exploiting the linear relationship between the equivalent initial flaw size and the parameter R_t [28]. Zhang and Fatemi adopted the maximum value R_v found from a set of measurements to perform linear elastic fracture mechanics calculations and successfully estimated multiaxial fatigue test results [29]. Nakatani et al. have re-adapted the formula valid for periodic surface notches, originally proposed by Murakami for machined surfaces [25], to AM as-built surfaces by equating the areal roughness parameter, S_z, to the depth of periodic circumferential cracks, and the R_{Sm} parameter to the pitch of the periodic cracks [30]. Despite the original equation proved accurate when assuming artificial periodic surface notches resulting from machining processes, the fatigue limit estimation of as-built SLM Ti6Al4V specimens by using an equivalent defect size calculated from S_z and R_{Sm} did not correlate the experimental results [30]. However, Barricelli and Beretta have recently shown that the periodic surface notches formula with the profile parameters R_v and R_{Sm} is still valid with acceptable approximation [31]. Moreover, some researchers have proposed new models for evaluating the fatigue strength of as-built AM materials starting from the linear elastic stress concentration factor evaluated by using S_v [32], or hybrid surface parameters [33], being the parameter S_v better related to the fatigue strength of AM materials with

random surface roughness than other surface roughness parameters [34].

As highlighted by Beretta [35], the measurements of R_v, R_t or S_v over a sampling length or control area correspond to a block maxima sampling. Therefore, the maximum value is related to the sampling length or control area inside which the measure is performed, according to the Extreme Value Statistics (EVS). Fox and Pintar support this approach inasmuch their findings show that the maximum value of S_v in a reference area of AM as-built surface can be accurately extrapolated from a small set of measurements by using a Gumbel distribution [36]. From a structural durability point of view, Computed Tomography (CT) analyses carried out on AM specimen subjected to cyclic loading revealed that nearly all specimens had cracks at the surface feature with the largest linear elastic Stress Intensity Factor (SIF), i.e. at the deepest valley of the surface [37]. The use of EVS applied to a subset of 2D areal measurements of the surface texture combined with fracture mechanics evaluations seems to be a promising approach for quantifying the influence of surface roughness on the fatigue behaviour of AM alloys and the present investigation supports this approach. The use of CT scan holds significant importance in the assessment of surface topography of AM materials due to the capability of detect re-entrant feature that cannot be measured by optical techniques [38]. However, CT measurements have some limitations regarding the assessment of surface textures of AM parts such as the need for a sample size of the millimetre scale for obtaining a voxel size of the micrometre scale, the high cost and the time-consuming procedure, along with significant data post-processing [39,40].

In this context, the present investigation explores the potential of optical techniques as a trade-off solution from an industrial perspective to evaluate surface roughness parameters useful for fatigue limit estimations by means of fracture mechanics approaches. Therefore, a fracture mechanics analysis has been performed to estimate the fatigue thresholds (hereafter intended as fatigue strength at 10^7 cycles) of as-built Ti6Al4V specimens using standardised areal parameters to define an effective surface crack size by using EVS. Three hypotheses were considered to derive the effective crack size: (i) periodic circumferential cracks having geometry defined by S_v and R_{Sm}, (ii) single circumferential crack having depth equal to S_v and (iii) single semi-circular crack having depth equal to S_v. These hypotheses were combined with the theoretical model proposed by Atzori, Lazzarin and Meneghetti [41–43], where the material properties were estimated by means of a recent empirical model proposed by Rigon and Meneghetti [44,45]. Eventually, theoretical estimations have been compared with experimental results. Furthermore, the prospective applicability of the 1D roughness profile parameter R_v combined with EVS is discussed and the resulting statistical estimation of the fatigue limit distribution is compared with the experimental results.

2. Theoretical background

2.1. Estimation of the fatigue thresholds

The dependence of the fatigue limit on the crack size was found by Kitagawa and Takahashi [46], who noted that for vanishingly small cracks the remotely applied threshold stress equals the fatigue limit of the defect-free material $\Delta\sigma_0$, while for long cracks the threshold condition of a constant range of the SIF holds true, namely $\Delta K_{th,LC}$. Fig. 1 interprets the two asymptotes originally observed experimentally [46] and reports also the El Haddad-Smith-Topper [24] and Murakami [25] models, which will be introduced later on, to estimate the fatigue thresholds for any intermediate crack size. The range of crack sizes in the transition region between very short and very long cracks highlighted in Fig. 1 is relevant to surface roughness asperities.

It is known that for a polished mirror-like steel, the defect-free fatigue limit $\Delta\sigma_0$ (expressed in MPa) for a load ratio, R, equal to -1 is proportional to Vickers hardness (expressed in kg_f/mm^2) [25]:

$$\frac{\Delta\sigma_{0(R=-1)}}{2} = 1.6HV \pm 0.1HV \tag{1}$$

where the symbol "Δ" is used to indicate the range (i.e., maximum value minus minimum value) of the considered quantity. Beside steels, such equation proved applicable also to wrought titanium alloys [25].

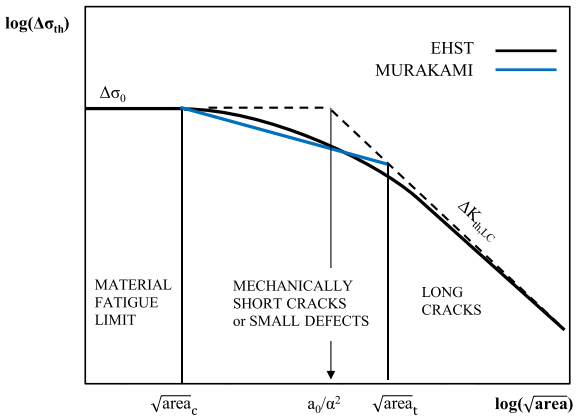

Fig. 1. Schematic representation of EHST and Murakami models.

Defects negatively affect the fatigue strength of metal materials proportionally to their size, defined by the square root of the projected area of the real volumetric defect in the plane normal to the maximum principal stress, $\sqrt{area}$. The fatigue limit of a material (identified by HV) decreases by increasing $\sqrt{area}$ and can be estimated by the following equation proposed by Murakami for $R = -1$ [25]:

$$\frac{\Delta\sigma_{g,th}}{2} = \frac{1.43 \cdot (HV + 120)}{\sqrt{area}^{1/6}} \tag{2}$$

where the units of $\Delta\sigma_{g,th}$, HV and $\sqrt{area}$ are [MPa], [kg_f/mm^2] and [μm], respectively, and the coefficient 1.43 is appropriate for surface defects. The general validity of the Murakami model (M−model), Eq. (2), in terms of $\sqrt{area}$ ranges from 10 μm to 1000 μm, but several investigations reported in the literature suggest to adopt more accurate lower and upper bounds of the model, which are defined by the critical $\sqrt{area}_c$ and the transition $\sqrt{area}_t$ lengths, respectively, as reported in Fig. 1 [47–49].

The first asymptote shown in Fig. 1, given by $\Delta\sigma_0$, can be estimated theoretically by means of Eq. (1), while the second one, which depends on the $\Delta K_{th,LC}$, can be estimated by taking advantage of an empirical equation recently proposed by Rigon and Meneghetti for different load ratios and a certain range of materials, including also AM titanium alloys [44,45]. More precisely, $\Delta K_{th,LC}$ for $R = -1$ can be estimated by means of the following equation:

$$\Delta K_{th,LC,(R-1)} = 4.5l^{0.127} + 2.29 \cdot 10^2 HV^{-0.81} \tag{3}$$

where l is a length parameter dependent on the material microstructure, and, in particular, is the average width of the α lamellae in the case of Ti6Al4V with α + β lamellar microstructure [44,45]. Units of $\Delta K_{th,LC,(R-1)}$, l and HV in Eq. (3) are [MPa $\sqrt{m}$], [μm] and [kg_f/mm^2], respectively.

El Haddad, Smith and Topper proposed a model where the dependence of the fatigue limit on the crack size is expressed by the following equation [23,24,50,51]:

$$\Delta\sigma_{th} = \Delta\sigma_0 \sqrt{\frac{a_D}{a + a_D}} \tag{4}$$

where a is the crack length and a_D is the characteristic length defined as follows:

$$a_D = \frac{1}{\alpha^2 \cdot \pi} \left(\frac{\Delta K_{th,LC}}{\Delta\sigma_0} \right)^2 \tag{5}$$

The non-dimensional shape factor α of Eq. (5) is adopted in fracture mechanics studies to define the linear elastic SIF:

$$K_I = \alpha\sigma_g \sqrt{\pi a} \tag{6}$$

and it is worth mentioning that the use of the shape factor α in the EHST model (Eq. (5)) is due to Du-Quesnay, Yu and Topper [50,51].

In the present paper, the following definition of the length parameter a_0, which depends only on material properties, is used according to the original paper by El Haddad, Smith and Topper [23,24], subsequently adopted by Atzori, Lazzarin and Meneghetti [41–43]:

$$a_0 = \frac{1}{\pi} \left(\frac{\Delta K_{th,LC}}{\Delta\sigma_0} \right)^2 \tag{7}$$

Coherently with the definition (7), the shape factor α was included in a so-called effective crack length a_{eff} defined by the SIF equality [42,43] Eq. (6):

$$a_{eff} = \alpha^2 a \rightarrow = \frac{1}{\pi} \cdot \left(\frac{K_I}{\sigma_g} \right)^2 \tag{8}$$

and Eq. (4) was updated according to the following expression:

$$\Delta\sigma_{th} = \Delta\sigma_0 \sqrt{\frac{a_0}{a_{eff} + a_0}} \tag{9}$$

Incidentally, the original approach proposed in ref. [41,42] has been later generalised in a unifying theoretical model to treat the mode I fatigue limit of open V-notches of any sharpness and size [43].

2.2. Definition of the effective crack size based on 2D areal parameters

The ALM model (Eq. (9)) can be applied by using appropriate definitions of the effective crack size. The first model to evaluate the effective crack size a_{eff} of the as-built surface follows Murakami's approach for machined surfaces (i.e., for a regular surface pattern), which adopts two parameters, namely the total height a and the pitch 2b of periodic notches idealised as cracks and schematically illustrated in Fig. 2(a) [25]. The equivalent defect size $\sqrt{area}_R$ to be used in Eqs (2), (4) and (9) can be evaluated by means of the

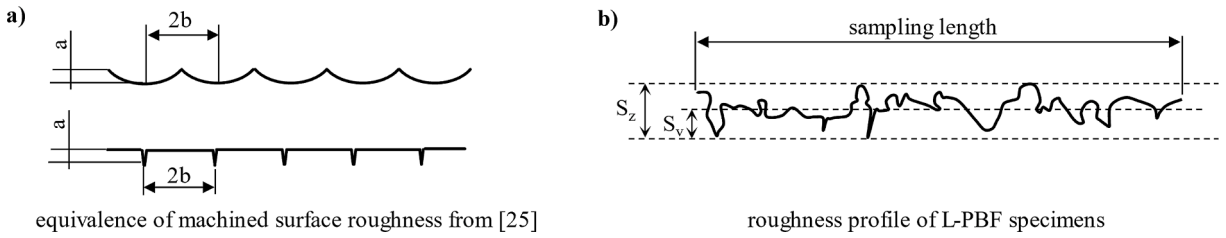

Fig. 2. (a) Schematic representation of periodic notches of a machined surface and its equivalence with periodic cracks. (b) Typical surface roughness profile of L-PBF samples.

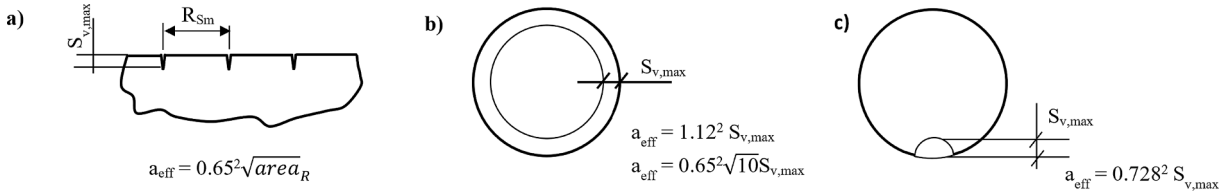

Fig. 3. Effective crack size of the surface roughness of AM materials assumed in the present study: (a) periodic circumferential cracks, (b) single circumferential crack and (c) single semi-circular crack.

following expressions [25]:

$$\begin{cases} \dfrac{\sqrt{area}_R}{2b} = 2.97\left(\dfrac{a}{2b}\right) - 3.51\left(\dfrac{a}{2b}\right)^2 - 9.74\left(\dfrac{a}{2b}\right)^3 & for \quad \left(\dfrac{a}{2b}\right) < 0.195 \\ \dfrac{\sqrt{area}_R}{2b} \cong 0.38 & for \quad \left(\dfrac{a}{2b}\right) \geq 0.195 \end{cases} \tag{10}$$

Typical surface roughness patterns of L-PBF parts are complex and irregular as reported in the 1D sketch reported in Fig. 2(b); consequently, some authors assumed (i) the parameter S_z to be a, being S_z the maximum height of the surface, and (ii) the mean spacing of profile elements R_{Sm} to be $2b$ in Eq. (10) [30]. However, the profile height of an as-built AM surface is basically influenced by partially melted/sintered particles that do not bear loads; therefore, according to [34] one should adopt the best fatigue-related 2D areal parameter, i.e. S_v, defined as the maximum pit depth measured from the reference plane of 2D areal measurements. On the contrary, it is worth noting that R_z, S_z or hybrid parameters would be more appropriate than R_v or S_v when the as-built surface is half-polished (i.e. hand-polished by abrasive paper to isolate the effects of the valleys), because in this case the height distribution is skewed [28,33]. In this paper, S_v has been chosen to be a in Eq. (10), and R_{Sm} to be $2b$ (Fig. 3(a)), being R_{Sm} the most suitable parameter that describes the valley-to-valley distance according to [25,34].

Finally, the effective crack size a_{eff} (Eq. (8)) can be expressed in terms of $\sqrt{area}$ by using the SIF equation proposed by Murakami [25]:

$$a_{eff} = \alpha^2\sqrt{area} \tag{11}$$

where α is equal to 0.65 for surface defects.

The second model to describe the AM surface texture with an effective crack size considers the deepest valley like a single circumferential crack, as reported in Fig. 3(b):

$$a = S_v \tag{12}$$

Alternatively, the expression proposed by Murakami for very shallow crack can be considered [25]:

$$\sqrt{area} = \sqrt{10}S_v \tag{13}$$

The third model takes the deepest surface irregularity as a semi-circular crack having depth S_v, as reported in Fig. 3(c), characterised by a shape factor α under pure tension equal to 0.728 according to the formulation by Newman and Raju [52]. It is worth noting that the semi-circular or semi-elliptical crack shape hypotheses have been adopted in several fracture mechanics studies of as-built AM materials [37,53–55].

Taking the relevant α for each model shown in Fig. 3, a_{eff} can be calculated by means of Eqs. (8) and (11), resulting in the following expressions, respectively:

$$a_{eff} = 0.65^2\sqrt{area}_R \tag{14}$$

$$a_{eff} = 1.12^2 S_v \approx 0.65^2 \sqrt{10} S_v \tag{15}$$

$$a_{eff} = 0.728^2 S_v \tag{16}$$

2.3. Extreme value statistics applied to 2D areal measurements

The largest S_v value in a reference area, A_{ref}, can be estimated by means of the extreme value statistics [56], starting from 2D areal measurements of the maximum pit depth (S_v) within individual control areas, each of them having size A_0; the approach is similar to the block maxima sampling to estimate the largest inclusion in a metal volume [25]. As demonstrated by Fox and Pintar [36], the distribution of S_v values evaluated individually within A_0, can be described by the Largest Extreme Value Distribution (LEVD), i.e. the Gumbel distribution [56], having the following equation:

$$F_{A_0}(S_v) = exp\left\{ - exp\left[- \frac{(S_v - \lambda)}{\delta} \right] \right\} \tag{17}$$

where $\delta > 0$ is the scale parameter and λ is the location parameters, that corresponds to the modal value of the distribution (36.8% percentile). By considering $u = -\ln(-\ln(F))$, the expression of the p-th percentile is the following:

$$S_v(p) = \lambda + \delta \cdot u \tag{18}$$

which is a linear relationship that can be used for representing the distribution in a probability plot.

The estimates of parameters $(\widehat{\lambda}, \widehat{\delta})$ can be calculated by means of (i) the linear interpolation of the data, (ii) the moments method or (iii) the maximum likelihood method. The best estimation of the parameters can be made by applying the last-mentioned method, as reported in [57,58]. However, the moments method has been applied in this study for the sake of a compromise between simplicity and accuracy, where $(\widehat{\lambda}, \widehat{\delta})$ can be estimated from the average $\mu(S_v)$ and standard deviation st.dev(S_v) of the measured S_v values [58]:

$$\mu(S_v) = \widehat{\lambda} + \gamma \widehat{\delta}$$

$$\text{st.dev}(S_v) = \frac{\pi}{\sqrt{6}} \widehat{\delta} \tag{19}$$

where γ is the Euler's constant (γ=0.5772).

Let us consider a specimen where n values of $S_{v,j}$ (j = 1,…,n) have been extracted from n-control areas, having size A_0. By ordering the $S_{v,j}$ in ascending order, the empirical probability, q_j, can be calculated by the following formulas:

$$q_j = \begin{cases} \dfrac{j}{n+1} & if\ n > 10 \\ \dfrac{j - 0.4}{n - 0.3} & if\ n \le 10 \end{cases} \tag{20}$$

The maximum value $S_{v,max,i}$, which is expected to be found on the entire surface of the gauge part of the i-th specimen, A_{ref}, has a return period:

$$T = \frac{A_{ref}}{A_0} \tag{21}$$

and it can be estimated by means of the following equation:

$$S_{v,max,i} = \widehat{\lambda} - \widehat{\delta} \ln\left(- \ln\left(1 - \frac{1}{T} \right) \right) \tag{22}$$

where $\widehat{\lambda}$ and $\widehat{\delta}$ are calculated by applying Eq. (19) to the available $S_{v,j}$ values of individual specimens.

A certain value $S_{v,max}$ can be estimated also for the entire test series of specimens by using Eqs (19) and (22) applied to all available $S_{v,j}$ values collected from all specimens of the test series, each of them analysed with control areas A_0. Such $S_{v,max}$ value of the test series is the modal value of the prospective distribution of $S_{v,max,i}$ obtained by block maxima sampling the test series of specimens using a control area equal to the entire surface of the gauge part of the specimen, A_{ref}. The corresponding graphical interpretation consists in moving downwards (along the ordinate axis) by the quantity $ln(T)$ the statistical distribution obtained by block maxima sampling with small control areas A_0, in order to obtain the statistical distribution based on block maxima sampling with control areas A_{ref}. It was observed that the latter distribution agrees with that obtained from the statistical analysis of the killer defects observed at the fracture origin of the test series of specimens [59]. Therefore, the distribution of S_v referred to A_{ref} can be estimated by means of the Gumbel distribution:

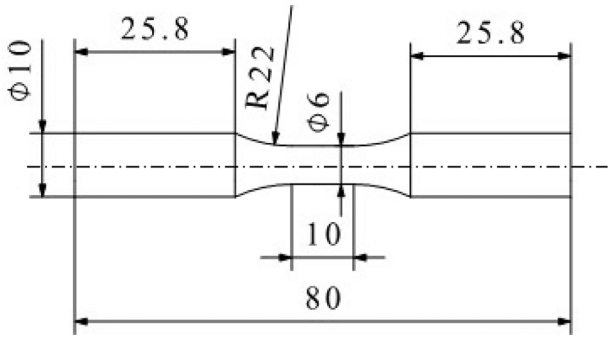

Fig. 4. Specimen's geometry (dimensions in mm).

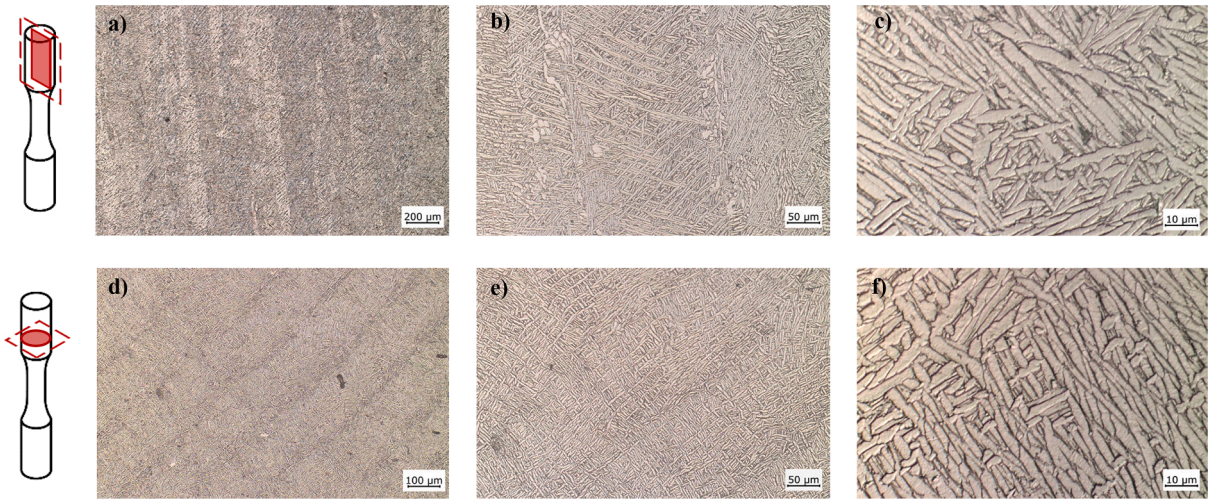

Fig. 5. Microstructure of the annealed Ti6Al4V samples in the longitudinal (a-c) and transverse (d-f) section of the specimen.

$$F_{A_{ref}}(S_v) = \left[F_{A_0}(S_v)\right]^T = \exp\left[-exp\left(-\frac{S_v - \lambda_{A_{ref}}}{\delta_{A_{ref}}}\right)\right] \tag{23}$$

where the parameters can be evaluated from those relevant to the distribution based on A_0, as follows:

$$\widehat{\lambda}_{A_{ref}} = \widehat{\lambda} + \widehat{\delta}\ln(T)$$

$$\widehat{\delta}_{A_{ref}} = \widehat{\delta} \tag{24}$$

Eventually, $F_{Aref}(S_v)$ is the distribution to be used for estimating the fatigue limit of the relevant batch of AM specimens by means of the M, EHST or ALM models.

The comparison between the theoretical fatigue thresholds and the experimental results will be based first on $S_{v,max,i}$ values estimated for individual specimens by using Eq. (22), while the fatigue limit estimation of the batch of AM specimens will be treated subsequently.

3. Material and methods

3.1. Material, specimens' geometry and microstructure

Cylindrical fatigue specimens with a 10-mm-long gauge section and nominal diameter equal to 6 mm were manufactured by means of selective laser melting using a MYSINT-100 system by SISMA S.p.a. The specimens were oriented in the built volume with their longitudinal axis parallel to the build direction (i.e., normal to the build platform) and their dimensions are reported in Fig. 4.

All specimens were annealed in vacuum at the temperature of 950 °C and then the two specimen ends were machined in a lathe (keeping the surface of the gauge part in as-built condition) to eliminate the process-induced geometrical distortions and thus avoid

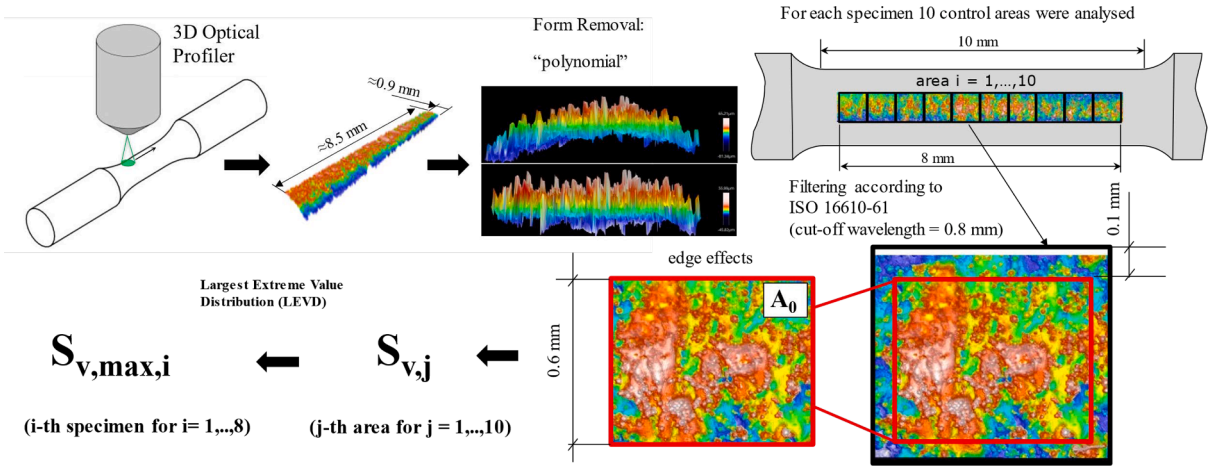

Fig. 6. Procedure for obtaining $S_{v,max}$ from 2D areal measurements on the gauge part of the i-th specimen.

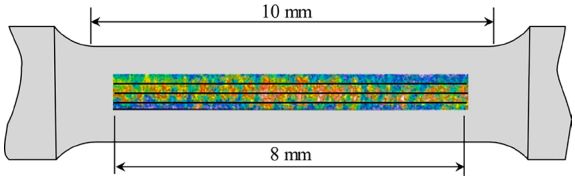

Fig. 7. 1D roughness profiles used for evaluating R_{Sm} for the i-th specimen.

uncontrolled secondary bending effects when the specimen is clamped by the fatigue testing grips. Further details regarding the heat treatment and the process parameters are omitted for confidentiality reasons.

A sample taken from the batch was used to analyse the material microstructure. Two sections were prepared, i.e., one parallel to the build direction and the second normal to the specimen axis, as schematically illustrated in Fig. 5. The Kroll reagent was used to etch the surfaces and reveal the microstructure. Afterwards, the sections were analysed by using an optical microscope, and the results are reported in Fig. 5. At low magnification the longitudinal section reported in Fig. 5(a) shows columnar grains parallel to the build direction, whereas the transverse section reported in Fig. 5(d) reveals the 150-μm-wide parallel traces of the laser scanning paths.

At higher magnifications, the lamellar microstructure α + β can be distinguished, where the α phase is shown in lighter colour, while the β phase is darker (Fig. 5(b, c, e, f)). The width of the α lamellae is the microstructural length parameter to use in Eq. (3) to estimate $\Delta K_{th,LC}$ [44,45] and was evaluated as mean value of 550 measurements performed on Fig. 5(c) by using the ImageJ® software.

A Leitz Vickers Microhardness indenter was used to measure the Vickers hardness at 10 points both on the longitudinal and the transverse sections previously used to analyse the microstructure; a total number of 20 measurements was performed according to the ISO-6507 standard [60]. Measurements were carried out along the radial direction and in such a way to have all measuring points at least 0.3 mm far from the external surface of the specimen, to comply with the ISO recommendations (the minimum distance from the external surface must be at least three times the mean diagonal length of the indentation, which resulted approximately 50 μm).

3.2. 2D areal measurements of the surface roughness parameters

The surface texture of the specimens was analysed by using an optical profiler Sensofar™ PLu-Neox equipped with an objective Nikon™ 20X EPI operating at 20 × magnification with a pixel size of 0.65 μm and z-axial measurement resolution of 0.02 μm. An area approximately equal to 0.88 × 8.52 mm^2 was analysed in the gauge part of the specimens using an automated linear travel along the longitudinal direction, as schematically reported in Fig. 6. Data acquisition and post-processing have been carried out using the SensoSCAN software (version 6.7).

First of all, a form removal tool available in SensoSCAN software called "polynomial" has been applied to the scanned surface to remove the curvature of the measured area. Afterwards, the following procedure has been applied for filtration, which separates (i) the waviness spatial component resulting from layer-by-layer manufacturing from (ii) the roughness spatial component of the optical surface measurement; this is the most challenging part of the process for determining the surface roughness parameters [32,33,39]. While the layer thickness adopted to manufacture the specimens has been omitted for confidentiality reasons, it is in the range of 10–50 μm according to the datasheet of the MYSINT-100 system. Owing to the interaction among several process parameters such laser power and layer thickness, the waviness caused by layer-by-layer manufacturing has generally one order of magnitude greater wavelength compared to the layer thickness [39]; therefore, in this case it is estimated in the range from 100 to 500 μm. In the present

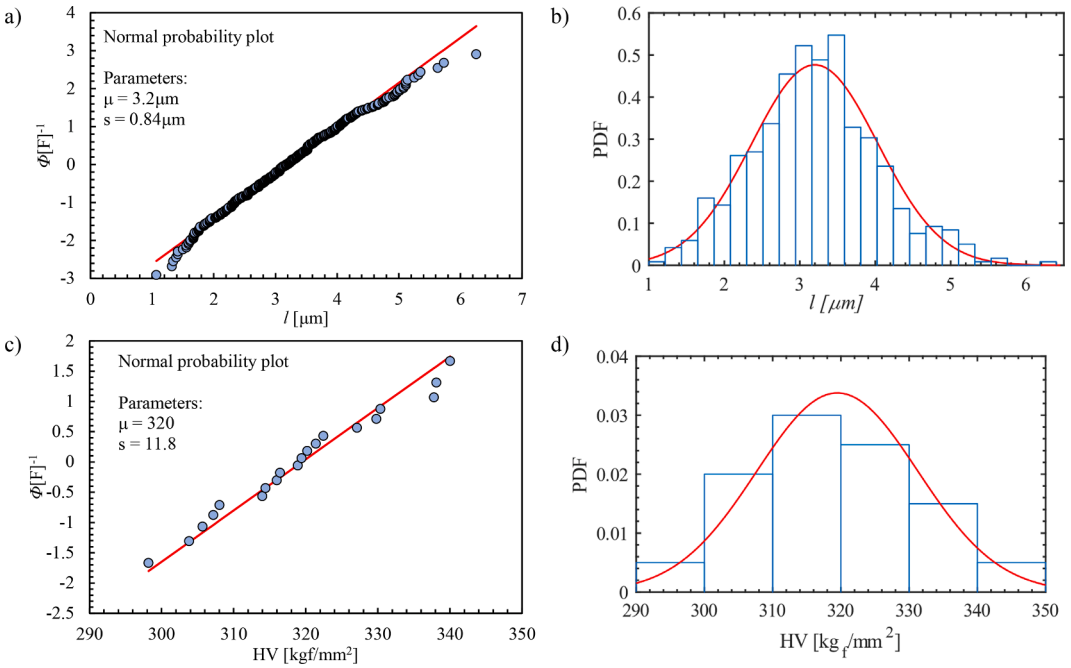

Fig. 8. Normal probability plot and probability density function of (a, b) the width of α lamellae and of (c, d) the Vickers hardness.

study a long-wave Gaussian filter with cut-off length (or nesting index) equal to 0.8 mm has been set, so that the waviness caused by the layer-by-layer manufacturing process has been likely kept after filtering. Following strictly the ISO 4288 recommendations [61], the appropriate long-wave cut-off filter for a prospective roughness parameter R_a in the range between 5 μm and 10 μm is 2.5 mm coupled with an evaluation length of 12.5 mm. This range of R_a values has been subsequently confirmed by performing 1D roughness profile measurements according to the concept illustrated in Fig. 7. Therefore, to make 1D roughness profile measurements consistent with 2D areal measurements, the nesting index filter of the latter should have a cut-off length of 2.5 mm as well. However, the experimental configuration of the available optical measuring system did not allow to analyse widths larger than 0.8 mm (see Fig. 6) which prevented using a nesting index of 2.5 mm for filtrating the 2D areal measurements. Owing to this restriction, the smaller 0.8 mm long-wave cut-off filter for 1D roughness profile and the same 0.8 mm nesting index for 2D areal measurements were selected in combination with ten 0.8 × 0.8 mm^2 sub-areas [27]. Subsequently, the sub-areas were reduced to the 0.6 × 0.6 mm^2 control areas A_0 by excluding a 0.1-mm-wide region around the boundary to avoid the edge effects caused by filtering (Fig. 6). Even though the size of the region of end effects was not in strict agreement with ISO 16610–61 recommendations [62], the error in truncating 0.1 mm with a 0.8 mm cut-off wavelength was deemed as negligible for the purpose of the work. The effect of the 0.8 mm nesting index on the resulting $S_{v,max}$ roughness parameter will be analysed in section 4.4.

To apply Eq. (10), the average R_{Sm} value was measured along three lines parallel to the direction of the specimens' axis (see Fig. 7). The R_{Sm} was evaluated starting from the optical profiler data by coding the crossing-the-line-segmentation algorithm [63] in a dedicated Matlab® script.

For the sake of completeness, the following 2D areal parameters were calculated in each j-th control area, A_0, by means of SensoSCAN® according to the definitions reported in ISO 25178 [27], even though only S_v will be considered in the subsequent analyses:

- ***S_q***: the root mean square (RMS) height parameter is the square root of the mean square of the ordinate values of the scale-limited surface; it is sometimes referred to as the RMS height:

$$S_q = \sqrt{\frac{1}{A}\iint_A z^2(x,y)dxdy} \tag{25}$$

- ***S_a***: the arithmetic mean height parameter is the mean of the absolute of the ordinate values of the scale-limited surface:

$$S_a = \frac{1}{A}\iint_A |z(x,y)|dxdy \tag{26}$$

- ***S_z***: the maximum height parameter is the sum of the maximum peak height value and the maximum pit depth value of the scale-limited surface.

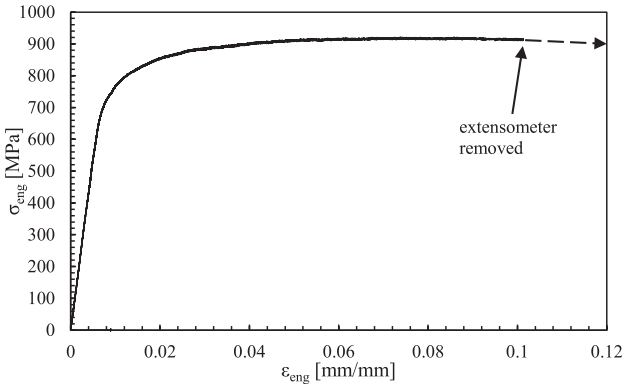

Fig. 9. Stress strain curve of the polished AM Ti6Al4V.

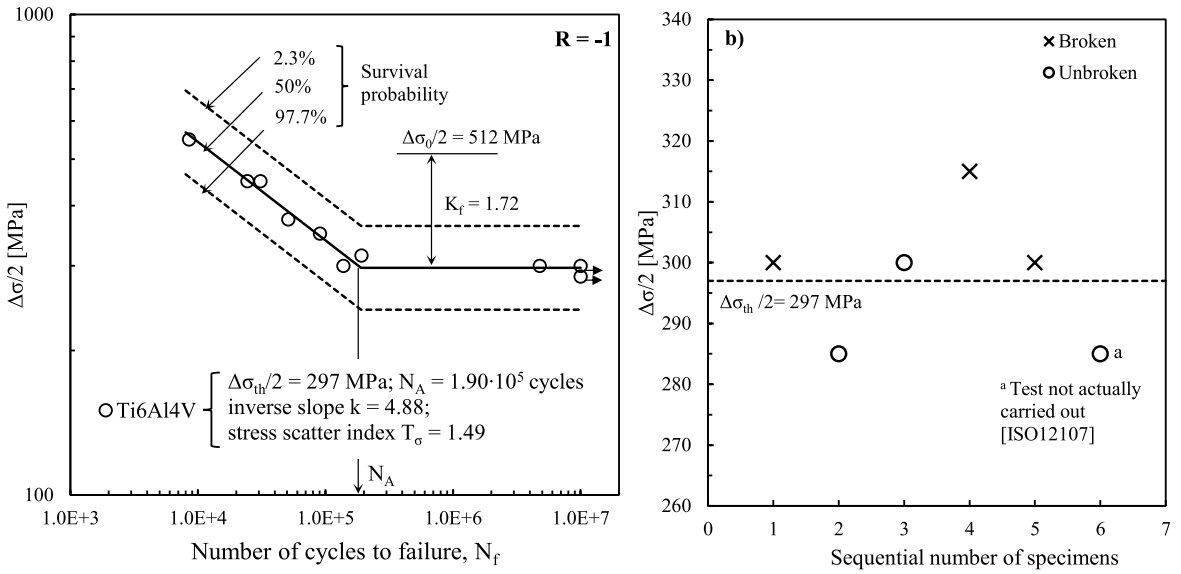

Fig. 10. (a) Fully reversed (R = -1) constant amplitude fatigue tests results expressed in terms of stress amplitude (i.e., $\Delta\sigma/2$) of Ti6Al4V specimens and fatigue curves for 2.3%, 50% and 97.7% survival probabilities. (b) Short staircase sequence at 10^7 cycles for determining the fatigue limit according to [64].

- ***Sp***: the maximum peak height parameter is the largest peak height value of the scale-limited surface
- ***Sv***: the maximum pit depth parameter is the largest pit depth value of the scale-limited surface (S_v must be taken as a positive quantity).

3.3. Testing procedures

The quasi-static mechanical properties of the material were determined with one tensile test after having polished the gauge part of the specimen by using emery paper until grade 1000. The tensile test was performed in displacement control mode with a rate equal to 0.25 mm/min by using a servo-hydraulic SCHENCK HYDROPULS PSA 100 machine having a 100 kN load cell and closed-loop digital controller TRIO Sistemi RT3. The engineering axial strain was measured by means of an MTS extensometer with a gauge length equal to 5 mm.

Constant-amplitude, load-controlled axial fatigue tests with load ratio R equal to -1 were carried out by using the same servo-hydraulic testing machine used for the tensile test. The load frequency was set in the range between 10 Hz and 30 Hz, depending on the applied load level. As aforementioned, all specimens were tested with as-built surface. Five specimens of the batch were used to evaluate the fatigue limit with run-out life at 10^7 cycles, according to the modified staircase method for small samples reported by ISO-12107 [64], which, strictly speaking, would have required six specimens. Finite life fatigue tests in the range from $5\bullet10^3$ to 10^6 cycles were used to evaluate the Wöhler curve and the relevant scatter band by statistical analysis of the collected data according to [64]. After fatigue testing, the fracture surfaces of the specimens were analyzed by using a ZEISS EVO MA10 Scanning Electron Microscope

Table 1
Estimated material properties at R = -1 from l and HV according to [44,45].

Material	Heat treatment	l [μm]	HV [kgf/mm^2]	$\Delta K_{th,LC}$ (Eq.3) [MPa$\sqrt{m}$]	$\Delta\sigma_0$^(Eq. (1)[MPa]	a_0 (Eq. (7)[μm]
Ti6Al4V	Annealing	3.2	320	7.36	1024	16.4

^Ideal defect-free plain material fatigue limit.

Table 2
Results of the quasi-static tensile tests.

Material	Heat treatment	E [GPa]	$\sigma_{y,0.2}$ [MPa]	σ_{UTS} [MPa]
Ti6Al4V	Annealing	110	742	922

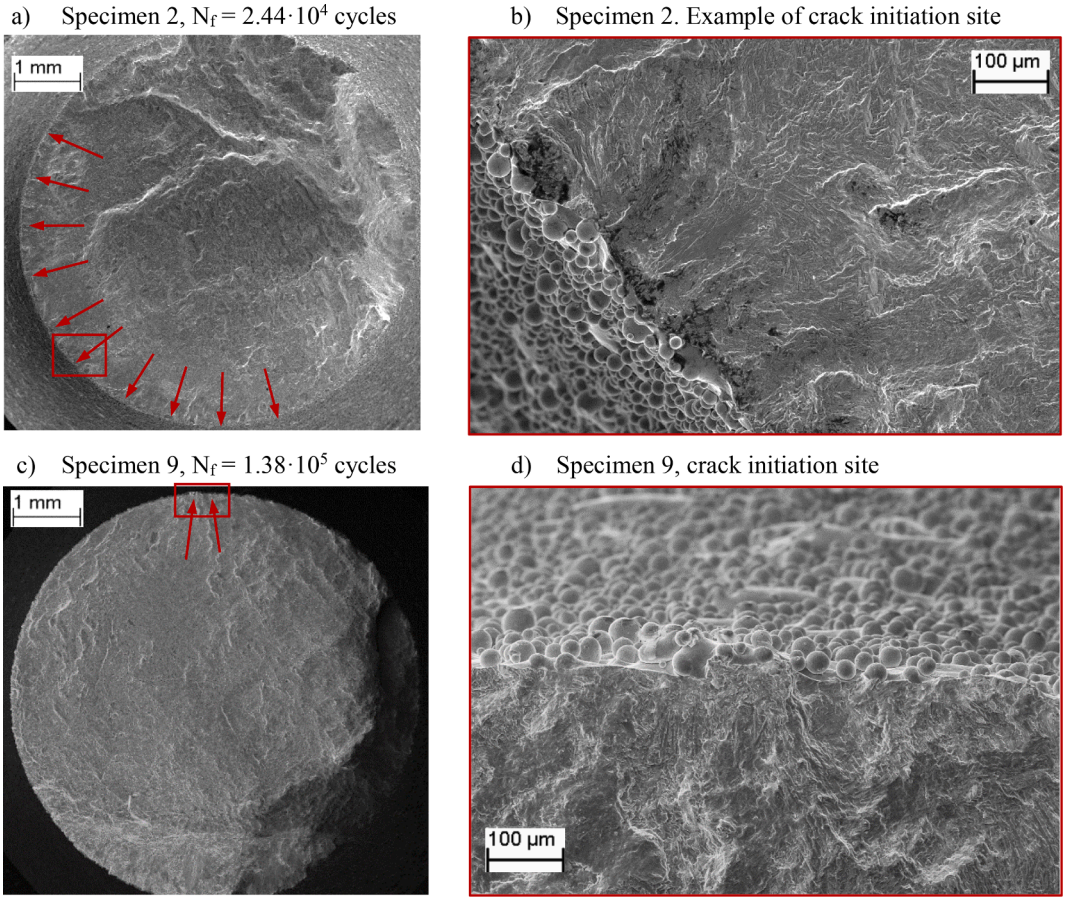

Fig. 11. (a) Fracture surfaces of specimens tested at high stress amplitude and (c) low stress amplitude; (b) and (d) report a magnification of a fatigue crack origin site of the previous images, respectively.

to examine closely the crack initiation locations.

4. Estimation of the fatigue limit of am specimens with as-built surfaces

4.1. Estimating $\Delta\sigma_0$ and $\Delta K_{th,LC}$

The measured widths of the α lamellae, taken from Fig. 5(c), are reported in the normal probability plot shown in Fig. 8(a) and in the histogram reported in Fig. 8(b). The data are well distributed over the linearised normal probability function Φ, characterised by an average value, μ, equal to 3.2 μm and a standard deviation, s, equal to 0.84 μm. Similarly, the 20 measured hardness values $HV_{0.5}$ expressed in kg$_f$/mm^2 are summarised in Fig. 8(c) and 8(d), where the average value and standard deviation of the normal distribution

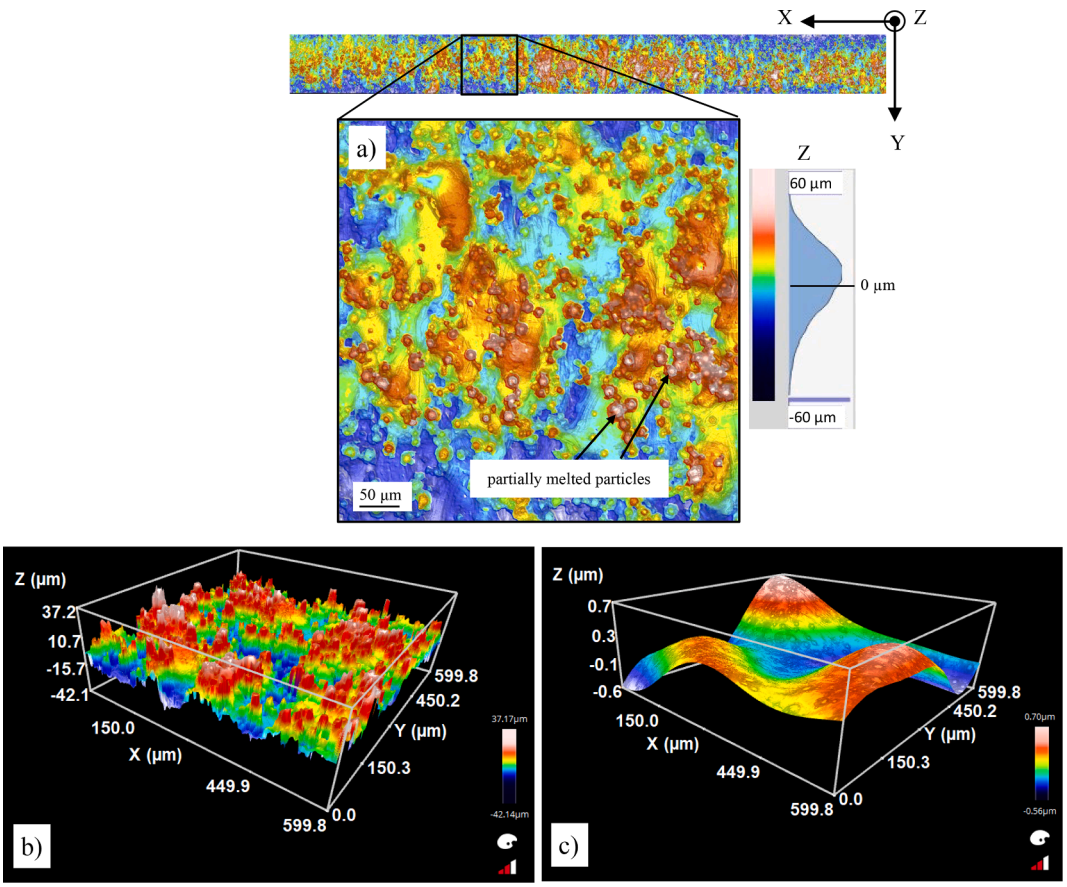

Fig. 12. (a) Example of surface acquisition by using the optical profiler; (b) roughness and (c) waviness components obtained by filtering according to ISO 16610–61 [62].

resulted 320 and 11.8 kg_f/mm^2, respectively.

From the average values of *HV* and *l*, the fatigue limit of the ideal defect-free material $\Delta\sigma_0$ and the threshold range of the SIF for long cracks $\Delta K_{th,LC}$ for R = −1 can be estimated by using Eqs. (1) and (3), respectively [44,45]. Results together with the EHST length parameter a_0, are summarized in Table 1.

4.2. Static and fatigue tests results

The tensile test performed on the polished specimen provided the material properties reported in Table 2 according to the stress–strain curve shown in Fig. 9. Percentage elongation after fracture according to ISO 6892–1:2016 [65] was not evaluated since the extensometer was removed before reaching its full-scale range, namely 10%.

Fatigue test results are reported in Fig. 10(a) in terms of nominal stress amplitude together with the fatigue curves for a survival probability, PS, of 2.3%, 50% and 97.7%, which were determined by statistical analysis of the experimental data relevant to seven broken specimens. The obtained inverse slope, *k*, and scatter index $T_{\sigma,2.3\text{-}97.7}$ are 4.88 and 1.49, respectively. The sloping part of the fatigue curve has been interrupted at the intersection with the fatigue limit $\Delta\sigma_{th}/2$, where the sequence of the staircase tests is reported in Fig. 10(b). The fatigue limit in terms of stress amplitude $\Delta\sigma_{th}/2$ resulted 297 MPa. The knee point at the intersection between $\Delta\sigma_{th}/2$ and the mean fatigue curve is seen to occur at a reference number of cycle N_A equal to $1.90 \bullet 10^5$. Finally, the scatter index $T_{\sigma,2.3\text{-}97.7}$ of the finite life region was applied also to the fatigue limit. By assuming the ideal defect-free plain material fatigue limit estimated from Eq. (1) (and reported in Table 1), the fatigue limit reduction factor K_f for this material and surface condition is $1024/(2 \cdot 297) = 1.72$.

4.3. Fracture surface analysis

Some exemplary images of fracture surfaces, which are representative of the entire batch of tested specimens, are reported in Fig. 11. The fracture surfaces of specimens subjected to high and low load levels are shown in Fig. 11(a) and 11(c), respectively. Fig. 11 (a) and 11(c) illustrate that the failure mechanism consists of multiple crack initiation sites at the specimen's surface and afterwards the initiated cracks coalesce to form larger cracks. The main difference of the initiation mechanism between high and low cyclic load

Table 3
Surface roughness parameters evaluated on the as-built AM specimens on each control area.

ID	d_{spec}* [mm]	A_{ref} [mm^2]	A_0 [mm^2]	$T = A_{ref}/A_0$	N° control area	S_q [μm]	S_a [μm]	S_z [μm]	S_p [μm]	S_v [μm]	R_{Sm} [μm]
3	5.95	186.6	0.36	519.2[§]	1	11.63	9.47	71.53	37.37	34.16	132.5
					2	11.16	8.96	71.28	36.64	34.64	
					3	11.14	9.27	68.18	36.43	31.74	
					4	9.52	7.67	87.86	58.76	29.10	
					5	10.45	8.54	77.16	43.96	33.20	
					6	10.07	8.05	66.84	36.21	30.63	
					7	9.23	7.32	65.95	31.68	34.27	
					8	9.28	7.34	66.56	36.64	29.92	
					9	9.43	7.50	65.13	31.47	33.66	
					10	11.30	9.11	80.27	46.26	34.02	
4					1	9.94	7.84	64.70	34.92	29.78	100.7
					2	10.13	8.27	68.31	36.52	31.79	
					3	9.54	7.72	60.59	34.77	25.82	
					4	9.78	8.15	60.47	35.80	24.66	
					5	10.59	8.43	82.47	53.18	29.29	
					6	9.65	7.81	67.02	39.43	27.59	
					7	9.32	7.53	73.11	37.55	35.55	
					8	8.90	7.39	58.29	30.39	27.91	
					9	8.36	6.95	54.42	29.74	24.68	
					10	8.76	7.09	66.11	36.17	29.94	
5					1	10.07	8.16	70.16	36.01	34.16	166.8
					2	11.41	8.95	83.95	47.26	36.69	
					3	10.60	8.38	80.25	40.11	40.15	
					4	9.99	7.88	76.57	38.97	37.60	
					5	9.74	7.60	66.86	35.59	31.27	
					6	10.17	8.03	74.16	34.59	39.57	
					7	9.85	7.78	68.53	42.16	26.36	
					8	11.17	8.71	76.67	43.97	32.71	
					9	12.05	9.55	77.29	37.41	39.88	
					10	10.25	8.09	74.07	34.37	39.70	
6					1	11.06	9.17	74.09	34.03	40.06	125.7
					2	10.92	8.89	71.07	31.62	39.45	
					3	10.62	8.89	77.02	31.65	45.37	
					4	9.09	7.30	68.36	24.53	43.83	
					5	9.68	7.98	73.26	29.66	43.59	
					6	9.21	7.62	66.26	29.22	37.04	
					7	7.67	6.10	65.09	31.57	33.52	
					8	8.63	7.02	73.97	30.51	43.46	
					9^	7.48	5.31	149.45	25.81	123.64	
					10	7.06	5.30	63.08	30.29	32.79	
7					1	9.99	8.13	78.28	36.58	41.69	123.8
					2	9.59	7.70	71.76	35.25	36.51	
					3	10.14	8.28	67.39	30.42	36.97	
					4	10.46	8.63	69.64	31.24	38.41	
					5	10.49	8.65	73.56	40.15	33.41	
					6	9.41	7.67	66.72	32.37	34.35	
					7	7.65	6.18	64.18	23.81	40.37	
					8	8.23	6.76	61.35	27.13	34.22	
					9	7.99	6.49	61.43	23.50	37.93	
					10	8.20	6.58	63.78	29.98	33.80	
8					1	10.08	8.18	79.31	37.18	42.14	143.0
					2	9.53	7.66	73.08	36.30	36.79	
					3	10.04	8.19	69.61	32.19	37.42	
					4	10.56	8.53	69.91	30.38	39.53	
					5	10.58	8.70	66.92	33.49	33.44	
					6	9.58	7.80	70.10	35.62	34.48	
					7	7.64	6.09	65.09	31.68	33.40	
					8	8.28	6.80	61.37	27.48	33.90	
					9	8.17	6.67	60.39	24.36	36.03	
					10	8.25	6.62	65.78	31.69	34.09	
9					1	11.15	9.16	86.39	35.93	50.46	112.8
					2	10.70	8.88	79.43	43.68	35.75	
					3	10.59	8.75	78.92	40.15	38.77	
					4	11.45	9.52	83.90	37.93	45.97	
					5	11.13	9.19	74.07	35.42	38.65	
					6	12.46	10.51	96.61	35.53	61.08	
					7	11.09	9.09	79.30	44.27	35.04	
					8	11.73	9.69	97.05	55.43	41.62	

(*continued on next page*)

Table 3 (*continued*)

ID	d_{spec}* [mm]	A_{ref} [mm^2]	A_0 [mm^2]	$T = A_{ref}/A_0$	N° control area	S_q [μm]	S_a [μm]	S_z [μm]	S_p [μm]	S_v [μm]	R_{Sm} [μm]
					9	11.61	9.71	87.95	42.15	45.81	
					10	11.20	9.25	82.94	45.32	37.62	
10					1	11.15	8.84	80.53	41.53	39.00	118.2
					2	11.22	9.03	83.67	42.30	41.37	
					3	10.28	8.34	67.11	35.22	31.89	
					4	12.36	9.55	77.33	48.89	28.44	
					5	10.43	8.54	75.03	46.47	28.55	
					6	10.42	8.50	66.88	38.39	28.49	
					7	10.23	8.49	60.27	34.20	26.07	
					8	9.89	7.94	63.43	32.59	30.84	
					9	9.35	7.68	61.53	35.18	26.35	
					10	10.07	8.10	61.19	32.55	28.64	

ˆOutlier excluded from the statistical analysis.

* Mean value of the actual specimen's diameter measured on the gauge part.

§ A_{ref} calculated by using the d_{spec}.

levels is the number of crack initiation sites or, equivalently, the circumferential region occupied by the crack initiation sites. More precisely, fracture surfaces originating from higher cyclic load levels are characterised by a larger number of crack initiation sites compared to lower load levels, as reported in Fig. 11(a) and Fig. 11(c), respectively. Furthermore, Fig. 11 shows that specimens tested at low load levels present a very limited extension of the failure-initiation area, which led to the assumption that the failure originated from a single initiation site. Fig. 11(b) and Fig. 11(d) report a magnification of the initiation sites identified in previous Fig. 11(a) and Fig. 11(c), respectively.

The fracture surfaces indicate that the fatigue failures originated from the asperities/micro notches of the as-built surface which are typical of L-PBF processes; instead, sub-surface defects were not detected in the crack initiation regions after observation of the fatigue fracture surfaces. Therefore, only the as-built surface analysis is appropriate in the present investigation, which involves high quality AM specimens. However, generally speaking, sub-surface defects may be present in AM specimens and trigger fatigue failure, which can be assessed using Fracture Mechanics approaches according to the literature [25,66,67].

4.4. 2D areal roughness parameters

Fig. 12(a) reports an exemplary measurement performed by the optical profiler on the gauge part of a specimen after having applied the form removal. The colour bar represents the linear z-coordinate of the surface ranging from −60 to +60 μm. The magnified area of Fig. 12(a) highlights the surface features commonly observed in as-built AM specimens, namely (i) the wavy pattern caused by solidification of the material layers and (ii) the partially melted particles [39]. To better illustrate the separation of the roughness component from the waviness component of the surface texture, a control area of the specimen n° 8 was re-analysed and the results obtained from Sensofar® software are presented in Fig. 12(b) and (c). Fig. 12(b) is the roughness component and it has been obtained as aforementioned, namely by applying the 0.8 mm long-wave nesting index filter (the filter eliminates all wavelengths greater than 0.8 mm), while Fig. 12(c) shows the associated waviness component (here the filter eliminates all wave lengths lower than 0.8 mm). The color-coded maps of the two patterns clearly show the wavelengths and the magnitudes (Z coordinate) of the two components.

The measured areal parameters listed in section 3.2 for each control area and specimen are reported in Table 3.

Fig. 13(a) shows the $S_{v,j}$ data (listed in Table 3) for each specimen with the relevant Gumbel distribution and the evaluated 95% confidence bands. All points are quite well linearly distributed in the graphs according to the literature [36]. By using Eq. (22) with the return period calculated as the ratio of the entire surface of the gauge part of the specimens A_{ref} ($A_{ref} = \pi \cdot 5.95 \cdot 10 \rightarrow = 186.92$ mm^2), and the control area A_0 ($A_0 = 0.6 \cdot 0.6 \rightarrow = 0.36$ mm^2), the $S_{v,max,i}$ value of the i-th specimen was calculated and is reported in Fig. 13(a).

To evaluate the impact of the adopted long-wave nesting index filter on the estimated $S_{v,max}$, after applying the polynomial form removal, the ten control areas of specimen n° 8 have been analysed with and without using the filter, respectively. Fig. 13(b) reports the results obtained in terms of LEVDs and highlights that the $S_{v,max}$ values obtained from the filtered and unfiltered data are approximately the same.

This result and the previously reported considerations suggest that the layer-by-layer waviness has been kept after filtering and has a negligible influence on the estimated $S_{v,max}$ value. Therefore, the use of a 0.8 mm long-wave nesting index filter, rather than the 2.5 mm filter suggested by the ISO standards, has not modified significantly the results of the present investigation.

4.5. Comparisons between estimated and experimental fatigue thresholds

Table 4 summarizes the largest pit depth within A_{ref} ($S_{v,max}$) and the mean spacing (R_{Sm}) evaluated from the surface roughness parameters of each specimen, together with the relevant effective crack size a_{eff} according to the Eqs. ((10),14–16). It is interesting that all specimens have $S_{v,max,i}/R_{Sm}$ ratio greater than 0.195, therefore the $\sqrt{area}_R$ parameter depends only on R_{Sm} (Eq. (10)). By comparing a_{eff} evaluated from the periodic (Eq. (14)) and single circumferential crack (Eq. (15)) models, the latter is on average 3.30 times greater than the former and it is also $(1.12/0.728)^2 = 2.37$ greater than estimated by using the single semi-circular crack model (Eq. (16)).

The comparison between experimental data and the theoretical fatigue thresholds is reported in Fig. 14, where open markers refer

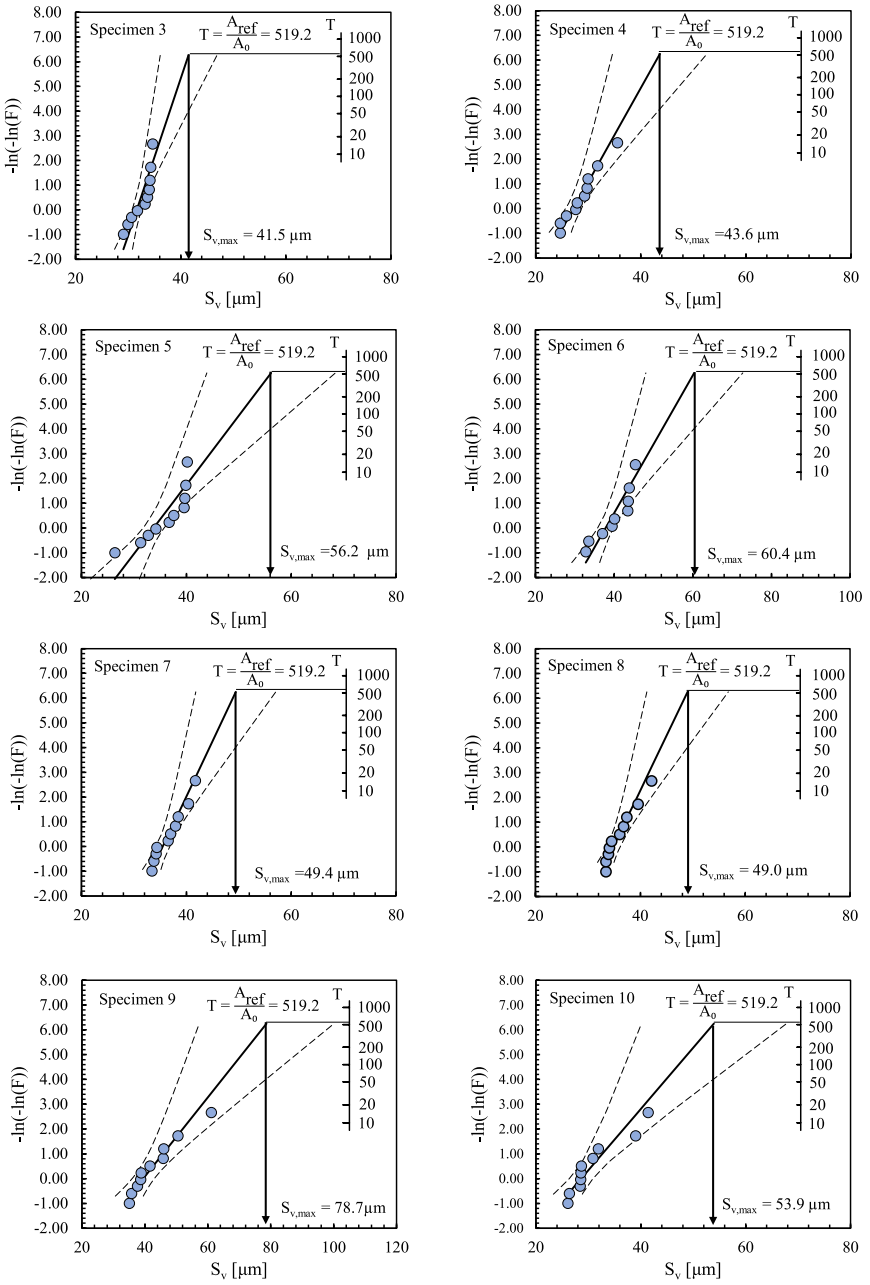

Fig. 13a. $S_{v,max,i}$ values of each specimen starting from the estimated LEVD and a return period T equal to $A_{ref}/A_0 = 519.2$. The $S_{v,j}$ data were acquired inside control areas A_0 0.6 mm x 0.6 mm. The scatter is referred to the 95% confidence bands.

to fatigue specimens failed before 10^7 cycles, while filled markers represent run-out specimens. The ALM model estimated with the material properties reported in Table 1 has been plotted with a constant stress-based scatter with scatter index equal to that obtained from the statistical analyses of the S-N data (see Fig. 10), namely $T_\sigma = 1.49$. If the correlations between theory and experiments were perfect, the ALM model should separate sharply the data relevant to failed and run-out specimens at 10^7 cycles.

According to Fig. 14(a), the periodic cracks assumption used in the ALM model correlates the experimental results with a certain degree of non-conservatism, since some data points of failed specimens fall below the line of the theoretical model. On the contrary, the circumferential crack hypothesis leads to certain degree of conservatism, as highlighted in Fig. 14(b). A good correlation is obtained by adopting the semi-circular crack hypothesis since failed and run-out data are well separated by the mean curve of the ALM model reported in Fig. 14(c). For appreciating the goodness of estimation of the maximum a_{eff} from areal measurements, Fig. 14(b) and 14c report the 95% confidence bands of the evaluated $S_{vmax,i}$ by means of EVD (see Fig. 13(a)).

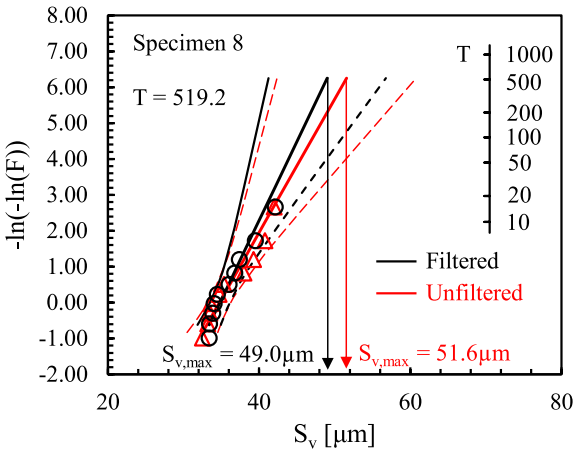

Fig. 13b. Comparison of the $S_{v,max}$ obtained from filtered and unfiltered data for the specimen n° 8.

Table 4
Effective crack size according to Eqs ((10),14–16) of each tested specimen.

						Periodic cracks*			Circumferential crack°		Semi-circular crack^	
ID	Δσ [MPa]	N_f [cycles]	$S_{v,max}$ [µm]	R_{Sm} [µm]	$S_{v,max}/R_{Sm}$	α	$\sqrt{area}_R$[µm]	a_{eff} [µm]	α	a_{eff} [µm]	α	a_{eff} [µm]
1	600	$4.78{\cdot}10^6$	/	/		/	/	/		/	/	
2	900	$2.44{\cdot}10^4$	/	/		/	/	/		/	/	
3	750	$5.10{\cdot}10^4$	41.5	132.5	0.313	0.65	50.4	21.3	1.12	52.1	0.728	22.0
4	570	10^7	43.6	100.7	0.433		38.3	16.2		54.7		23.1
5	900	$3.09{\cdot}10^4$	56.2	166.9	0.337		63.4	26.8		70.5		29.8
6	600	10^7	60.4	125.7	0.481		47.8	20.2		75.8		32.0
7	700	$9.04{\cdot}10^4$	49.4	123.8	0.399		47.0	19.9		62.0		26.2
8	630	$1.91{\cdot}10^5$	49.0	143.0	0.343		54.3	23.0		61.5		26.0
9	600	$1.38{\cdot}10^5$	78.7	112.9	0.697		42.9	18.1		98.7		41.7
10	1100	$8.50{\cdot}10^3$	53.9	118.2	0.456		44.9	19.0		67.6		28.6

*Eqs. (10) and (14).
° Eq. (15).
^Eq. (16).

5. Discussion

Fig. 14 reports the maximum effective crack size statistically evaluated by means of the relevant Gumbel distributions shown in Fig. 13(a). Being this size the maximum estimation on the entire surface of the gauge part of each specimen, it should be also correlated with the size of the killer defect, which is usually identified by analysing the fracture surface at the crack initiation site. However, on looking over Fig. 11(b) and 11(d), finding the asperity size of the as-built surface that triggered crack initiation is a tricky problem, owing to the very irregular as-built surface texture containing partially melted particles. Since the semi-circular crack assumption coupled with the ALM model proved effective for an engineering estimation of the fatigue thresholds, such hypothesis was adopted for analysing the entire batch of the specimens.

5.1. Estimation of the fatigue limit of the batch of specimens

Previous Fig. 14 presented the experimental data in terms of applied stress range coupled with the estimated killer defect size of individual specimens and compared them with the estimated fatigue thresholds according to the ALM model. However, if the aim of the analysis is the fatigue limit estimation of the entire batch of specimens, the statistical analysis should consider the S_v data acquired from all considered specimens, and specifically 10 measured values times 8 specimens, i.e., 80 S_v values. The Gumbel distribution of all available S_v values, $F_{A0}(S_v)$ found by adopting control areas A_0 and the corresponding probability density function $f_{A0}(S_v)$ are reported in Fig. 15(a). Starting from the distribution $F_{A0}(S_v)$, thanks to Eqs. (23) and (24) and making use of the return period T, it is possible to obtain the distribution of the S_v values in the larger reference area A_{ref}, $F_{Aref}(S_v)$, equal to the entire surface of the gauge part of the specimens, where $T = A_{ref}/A_0 \rightarrow 519.2$. The results are reported in Fig. 15(a). As aforementioned, it consists in shifting the Gumbel distribution $F_{A0}(S_v)$ downwards by the quantity $ln(T) = ln(A_{ref}/A_0)$; correspondingly, the probability density function $f_{A0}(S_v)$ moves towards the right. The resulting $F_{Aref}(S_v)$ and $f_{Aref}(S_v)$ reported in Fig. 15(a) represent the statistical estimation of the size distribution of the killer defects. This approach is consistent with previous investigations that demonstrated the good agreement between the Gumbel

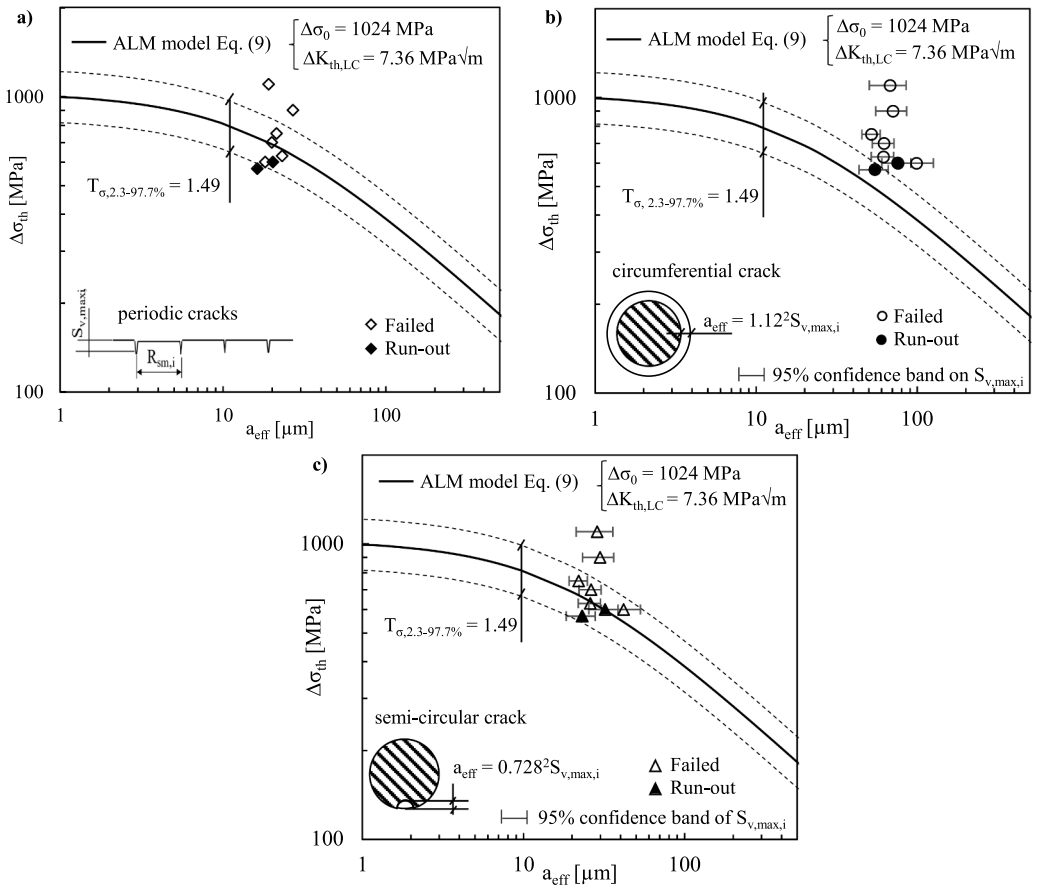

Fig. 14. Correlation between the ALM model and the experimental fatigue data evaluated according to the three models of the effective crack size (Eqs.(10,14–16)). Scatter band of the ALM model relevant to 2.3%-97.7% PS obtained from Fig. 10.

distribution of the killer defects observed on the fatigue fracture surfaces of a batch of specimens and that obtained by shifting the distribution of the maximum defect sizes determined by the method of polished sections on the specimens [59].

The lower bound of the fatigue limit can be estimated by evaluating the corresponding $S_{v,UpperBound}$ from $F_{Aref}(S_v)$ with a return period equal to a number of specimens $T = 100$ [68] (Fig. 15(a)). Interestingly, the same $S_{v,UpperBound}$ can be determined by considering $F_{A0}(S_v)$ and a return period $T = N{\cdot}A_{ref}/A_0$, where N is the number of specimens [25].

From the point of view of fatigue design, it is interesting to evaluate the probability density function of the estimated fatigue limit, hereafter called $f_{a_{eff}}(\Delta\sigma_{g,th})$, obtained from the statistical distribution of the effective crack size, $f_{A_{ref}}(a_{eff})$, by way of the function $\Delta\sigma_{th} = g(a_{eff})$, where g is the ALM model (Eq. (9)) and $f_{A_{ref}}(a_{eff})$ can be easily obtained from $f_{Aref}(S_v)$, being $a_{eff} = 0.728^2{\cdot}Sv$. By indicating $a_{eff} = g^{-1}(\Delta\sigma_{th}) = h(\Delta\sigma_{th})$, then $f_{a_{eff}}(\Delta\sigma_{th})$ can be evaluated as follows [69]:

$$f_{a_{eff}}(\Delta\sigma_{th}) = f_{A_{ref}}(h(\Delta\sigma_{th})) \cdot |h'(\Delta\sigma_{th})| \tag{27}$$

where h' is the derivative of $h(\Delta\sigma_{th})$ with respect to $\Delta\sigma_{th}$. Fig. 15(b) shows the ALM model, the experimental fatigue limits evaluated for 2.3%, 50% and 97.7% survival probabilities reported on the y-axis and the probability density function of the effective size $f_{Aref}(a_{eff})$ reported on the x-axis. Then, $f_{Aref}(a_{eff})$ has been mapped onto the y-axis to estimate the corresponding p.d.f. of the fatigue limit $f_{a_{eff}}(\Delta\sigma_{g,th})$ according to Eq. (27). Furthermore, the 2.3%-97.7% experimental scatter band of the fatigue limit has been mapped from the y-axis onto the x-axis and the corresponding range of a_{eff} values has been indicated in the figure. From a qualitative perspective, the p.d.f. of a_{eff} and $\Delta\sigma_{g,th}$ are in good agreement with the corresponding 2.3%-97.7% survival probability scatter band. In particular, it is interesting to note that the estimated fatigue limit by means of a 50th percentile of a_{eff} distribution ($a_{eff,50\%}$= 34.3 µm) is equal to 583 MPa, i.e., very close to the experimental value evaluated for survival probability of 50 % (594 MPa), with a percentage difference of only −1.9%, in agreement with a recent investigation [70]. Moreover, Fig. 15(b) shows that the probability density function of the effective size $f_{Aref}(a_{eff})$ is narrower than the scatter band determined by mapping the experimental scatter band of the fatigue limit onto the x-axis. However, it should be kept in mind that the experimental scatter band of the fatigue limit has not been determined with dedicated fatigue tests, as reported in previous section 4.2.

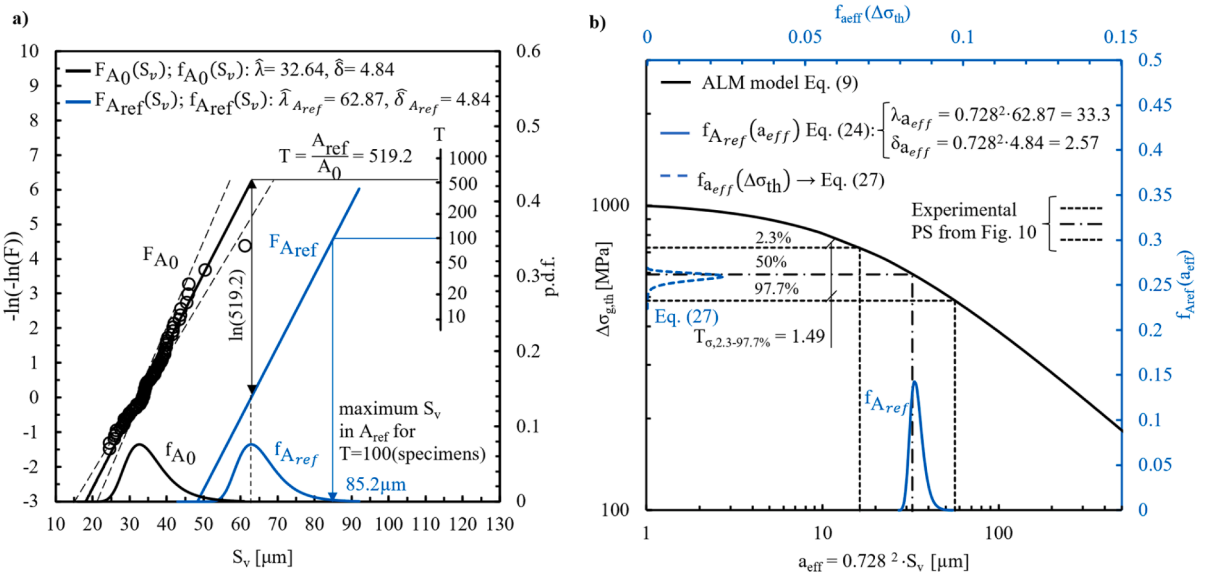

Fig. 15. (a) Gumbel distributions and probability density functions determined by (i) block maxima sampling S_v within A_0 (all S_v data in Table 3) and (ii) estimated for the reference area A_{ref}. (b) Comparison of the p.d.f. $f_{A_{ref}}(a_{eff})$ and $f_{a_{eff}}(\Delta\sigma_{g,th})$ with the experimental scatter: the experimental scatter of $\Delta\sigma_{g,th}$ refers to 2.3–97.7% survival probability according to Fig. 10(a) and is mapped to a_{eff}; the p.d.f. of a_{eff} is mapped to $\Delta\sigma_{g,th}$ by means of Eq. (27).

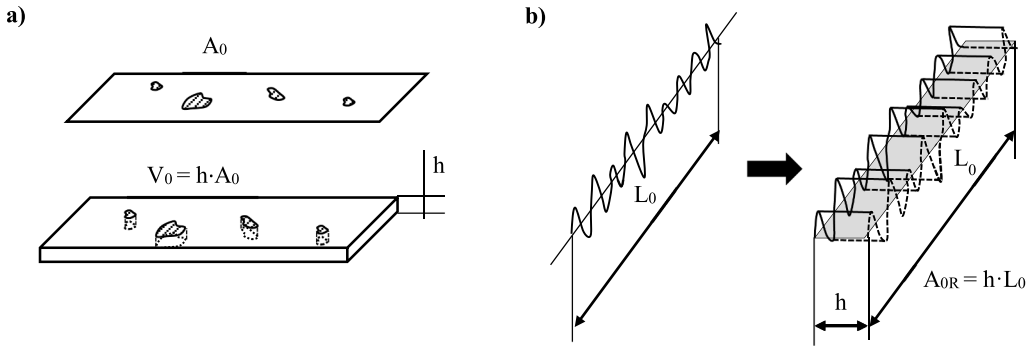

Fig. 16. (a) the method of polished sections and (b) its application to 1D line measurements.

5.2. Comparison between 2D areal domain and 1D roughness profile methods

Using 1D roughness profile measurements rather than 2D areal domain parameters may be faster and more affordable, therefore a procedure able to transfer 1D roughness profile measurements to 2D areal data is worth investigating.

The approach proposed in the following has been inspired by the method of polished sections proposed by Murakami to estimate the maximum defect size contained in a material volume by using the EVS [25]. According to this method, the control volume is evaluated as the product of the control area A_0 and the mean size, h, of all largest defects, each of them detected in a control area A_0 (Fig. 16(a)). This procedure proved effective and returned accurate estimations of the maximum defect size by means of the EVS [25].

Similarly, in the present study, it is proposed that 1D roughness profile measurements are related to a corresponding 2D control area which is obtained by multiplying the mean value of the R_v data, h, and the sampling length L_0, as reported in Fig. 16(b). To apply this approach, the three lines adopted for measuring R_{Sm} (see previous Fig. 7) have been used and each of them has been divided into ten 0.8-mm-long sampling lengths for extracting ten R_v values, respectively. Therefore, 30 R_v values have been obtained from each specimen and an overall number of 8x30 = 240 values have been used for the statistical analyses. The mean value h of all R_v data was 20.6 µm, therefore the assumed control area A_{0R} was equal to 0.8 × 0.0206 = 0.0165 mm^2. Fig. 17(a) shows the resulting Gumbel distribution ($F_{A0R}(R_v)$) and the probability density function ($f_{A0R}(R_v)$) of R_v.

Once again, the Gumbel cumulative distribution referred to the reference area ($F_{Aref}(R_v)$) was obtained from the corresponding $F_{A0R}(R_v)$ by means of Eqs. (23) and (24), by using a return period T equal to A_{ref}/A_{0R} = 186.92/0.0165 → = 1.132·10^4. The resulting $F_{Aref}(R_v)$ and $f_{Aref}(R_v)$ are reported in Fig. 17(a) and compared with the distributions obtained from S_v measurements, which have been reported in previous Fig. 15(a). It is worth noting that $R_{v,50\%}$ of $f_{Aref}(R_v)$ is 16 % lower than $S_{v,50\%}$ of $f_{Aref}(S_v)$, being the absolute values

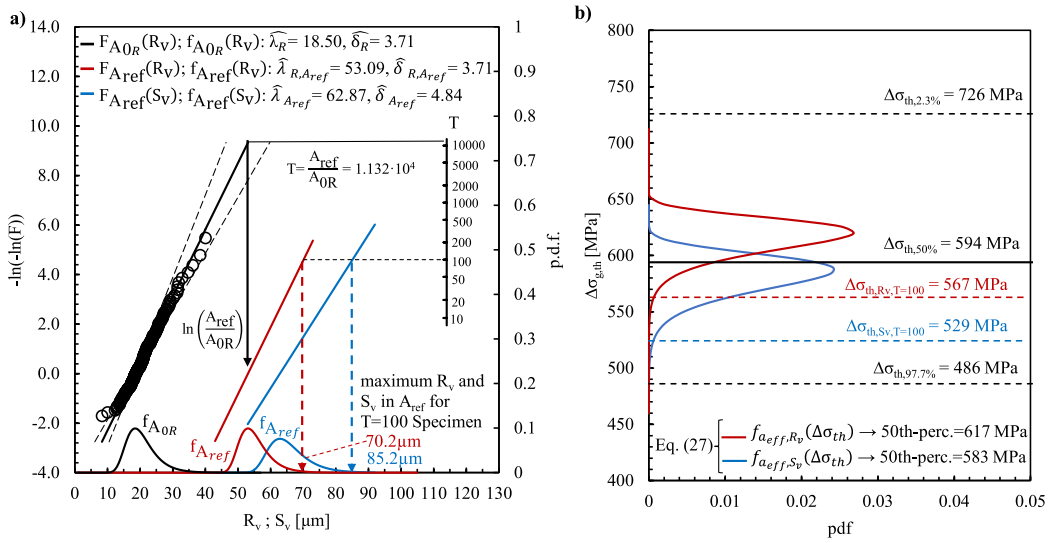

Fig. 17. (a) Gumbel distributions and probability density functions of R_v referred to the control (A_{0R}) and the reference (A_{ref}) areas, respectively; the latter is compared with the Gumbel distribution and probability density function based on S_v (from Fig. 15(a)). (b) Comparison of the estimated statistical distributions of the fatigue limit from R_v and S_v through the ALM model (Eq. (27)) with the experimental scatter of the fatigue limit. The lower bounds of the fatigue limit determined with T = 100 are also reported for the purpose of comparison with the experimental fatigue limit $\Delta\sigma_{th,97.7\%}$.

equal to 54.5 µm and 64.7 µm, respectively.

The fatigue limit has been estimated by mapping the pdf of R_v and S_v, respectively, through the ALM model, again by using Eq. (27). The results are reported in Fig. 17(b) and it is seen that the estimated fatigue limit from $a_{eff,50\%} = 0.728^2 R_{v,50\%} \rightarrow = 28.9$ µm (617 MPa) agrees with the experimental fatigue limit for survival probability of 50% (594 MPa), with a percentage difference of only + 3.8%. The lower bounds of the fatigue limit estimated with $R_{v,UpperBound}$ and $S_{v,UpperBound}$ (for 100 specimens) are equal to 567 MPa and 529 MPa, respectively, thus 17% and 9% greater than the fatigue limit for survival probability of 97.7% (486 MPa).

Finally, it should be noted that, despite the percentage difference between $R_{v,50\%}$ and $S_{v,50\%}$ is 16 %, the difference between the estimated fatigue limits in terms of 50th percentile of $f_{a_{eff},R_v}(\Delta\sigma_{th})$ and $f_{a_{eff},S_v}(\Delta\sigma_{th})$ is only 6% (617 MPa and 583 MPa, respectively). Therefore, the results reported in Fig. 17(b) seems to support the applicability of the approach proposed in this section, consisting in using 1D roughness profile measurements combined with the extreme value statistics for the fatigue limit estimation of as-built surfaces of AM metal materials.

6. Conclusions

In this study, the push–pull fatigue thresholds of AM Ti6Al4V alloy specimens with failure starting from the as-built surface were estimated by means of a fracture mechanics approach and compared with experimental results. The Atzori, Lazzarin and Meneghetti (ALM) model has been adopted, where two material properties are required, namely the defect-free plain material fatigue limit and the threshold range of the stress intensity factor for long cracks. The latter was estimated by means of a recently proposed empirical model, which is based solely on Vickers hardness and a microstructure-related length parameter. The effective crack size required by the ALM model is associated to the surface roughness and was estimated starting from optical areal measurements of the maximum pit depth S_v within well-defined control areas A_0 of the specimens. Then, the maximum value of S_v expected on the entire surface of the gauge part of the specimen has been estimated by using the extreme value statistics. The effective crack size associated to the maximum value of the pit depth S_v has been evaluated according to three different geometrical hypotheses: (i) periodic circumferential cracks, (ii) single circumferential crack and (iii) single semi-circular crack. According to a simplified approach, also 1D roughness profile measurements have been executed and the largest extreme value distribution of the relevant 1D parameter, R_v, has been compared with the corresponding statistical distribution of the 2D areal parameter, S_v. The following main conclusions can be drawn:

- the best correlation between the ALM model and the experimental results of the individual specimens has been obtained by using the semi-circular crack hypothesis;
- starting from block maxima sampling the maximum S_v value within control areas A_0 of individual specimens, the largest extreme value distribution of the S_v parameter over the entire surface of the gauge part of the specimens was estimated for the entire batch (namely the entire test series); by translating the associated probability density function in terms of effective crack size and mapping it by way of the ALM model, the corresponding fatigue limit distribution has been evaluated; the resulting estimation of the fatigue limit by using the 50th percentile of the effective crack size is in excellent agreement with the experimental fatigue limit referred to survival probability of 50%, being the percentage difference of the theoretical estimation only 1.9% lower than the experimental result.
- the method proposed to transfer 1D roughness profile measurements to equivalent 2D areal measurements proved effective and

the resulting estimation of the fatigue limit by using the 50th percentile of the effective crack size led again to a very good estimation, being the theoretical estimation only 3.8% greater than the experimental result.

CRediT authorship contribution statement

D. Rigon: Methodology, Data curation, Writing – original draft, Writing – review & editing. **F. Coppola:** Data curation, Investigation. **G. Meneghetti:** Conceptualization, Methodology, Validation, Investigation, Supervision, Writing – review & editing.

Declaration of Competing Interest

The authors declare that they have no known competing financial interests or personal relationships that could have appeared to influence the work reported in this paper.

Data availability

Data will be made available on request.

Acknowledgements

The authors would like to thank Prof. E. Savio and co-workers of the Department of Industrial Engineering (University of Padova) for the areal topography measurements.

References

[1] Gorelik M. Additive manufacturing in the context of structural integrity. Int J Fatigue 2017;94:168–77. https://doi.org/10.1016/j.ijfatigue.2016.07.005.
[2] Torries B, Imandoust A, Beretta S, Shao S, Shamsaei N. Overview on microstructure- and defect-sensitive fatigue modeling of additively manufactured materials. JOM 2018;70:1853–62. https://doi.org/10.1007/s11837-018-2987-9.
[3] Yadollahi A, Shamsaei N. Additive manufacturing of fatigue resistant materials: challenges and opportunities. Int J Fatigue 2017;98:14–31. https://doi.org/10.1016/j.ijfatigue.2017.01.001.
[4] Zerbst U, Bruno G, Buffière J-Y, Wegener T, Niendorf T, Wu T, et al. Damage tolerant design of additively manufactured metallic components subjected to cyclic loading: state of the art and challenges. Prog Mater Sci 2021;121:100786. https://doi.org/10.1016/j.pmatsci.2021.100786.
[5] Li P, Warner DH, Fatemi A, Phan N. Critical assessment of the fatigue performance of additively manufactured Ti-6Al-4V and perspective for future research. Int J Fatigue 2016;85:130–43. https://doi.org/10.1016/j.ijfatigue.2015.12.003.
[6] Meneghetti G, Rigon D, Cozzi D, Waldhauser W, Dabalà M. Influence of build orientation on static and axial fatigue properties of maraging steel specimens produced by additive manufacturing. Procedia Struct Integr 2017;7:149–57. https://doi.org/10.1016/j.prostr.2017.11.072.
[7] Rigon D, Meneghetti G, Görtler M, Cozzi D, Waldhauser W, Dabalà M. Influence of defects on axial fatigue strength of maraging steel specimens produced by additive manufacturing. MATEC Web Conf 2018;165:02005. https://doi.org/10.1051/matecconf/201816502005.
[8] Solberg K, Berto F. Notch-defect interaction in additively manufactured Inconel 718. Int J Fatigue 2019;122:35–45. https://doi.org/10.1016/j.ijfatigue.2018.12.021.
[9] Chern AH, Nandwana P, Yuan T, Kirka MM, Dehoff RR, Liaw PK, et al. A review on the fatigue behavior of Ti-6Al-4V fabricated by electron beam melting additive manufacturing. Int J Fatigue 2019;119:173–84. https://doi.org/10.1016/j.ijfatigue.2018.09.022.
[10] Carneiro L, Jalalahmadi B, Ashtekar A, Jiang Y. Cyclic deformation and fatigue behavior of additively manufactured 17–4 PH stainless steel. Int J Fatigue 2019;123:22–30. https://doi.org/10.1016/j.ijfatigue.2019.02.006.
[11] Afkhami S, Dabiri M, Alavi SH, Björk T, Salminen A. Fatigue characteristics of steels manufactured by selective laser melting. Int J Fatigue 2019;122:72–83. https://doi.org/10.1016/j.ijfatigue.2018.12.029.
[12] Damon J, Hanemann T, Dietrich S, Graf G, Lang K-H, Schulze V. Orientation dependent fatigue performance and mechanisms of selective laser melted maraging steel X3NiCoMoTi18-9-5. Int J Fatigue 2019;127:395–402. https://doi.org/10.1016/j.ijfatigue.2019.06.025.
[13] Kan WH, Nadot Y, Foley M, Ridosz L, Proust G, Cairney JM. Factors that affect the properties of additively-manufactured AlSi10Mg: porosity versus microstructure. Addit Manuf 2019;29:100805. https://doi.org/10.1016/j.addma.2019.100805.
[14] Razavi SMJ, Van Hooreweder B, Berto F. Effect of build thickness and geometry on quasi-static and fatigue behavior of Ti-6Al-4V produced by electron beam melting. Addit Manuf 2020;36:101426. https://doi.org/10.1016/j.addma.2020.101426.
[15] Wycisk E, Solbach A, Siddique S, Herzog D, Walther F, Emmelmann C. Effects of defects in laser additive manufactured Ti-6Al-4V on fatigue properties. Phys Procedia 2014;56:371–8. https://doi.org/10.1016/j.phpro.2014.08.120.
[16] Beretta S, Romano S. A comparison of fatigue strength sensitivity to defects for materials manufactured by AM or traditional processes. Int J Fatigue 2017;94:178–91. https://doi.org/10.1016/j.ijfatigue.2016.06.020.
[17] Masuo H, Tanaka Y, Morokoshi S, Yagura H, Uchida T, Yamamoto Y, et al. Influence of defects, surface roughness and HIP on the fatigue strength of Ti-6Al-4V manufactured by additive manufacturing. Int J Fatigue 2018;117:163–79. https://doi.org/10.1016/j.ijfatigue.2018.07.020.
[18] Yamashita Y, Murakami T, Mihara R, Okada M, Murakami Y. Defect analysis and fatigue design basis for Ni-based superalloy 718 manufactured by selective laser melting. Int J Fatigue 2018;117:485–95. https://doi.org/10.1016/j.ijfatigue.2018.08.002.
[19] Meneghetti G, Rigon D, Gennari C. An analysis of defects influence on axial fatigue strength of maraging steel specimens produced by additive manufacturing. Int J Fatigue 2019;118:54–64. https://doi.org/10.1016/j.ijfatigue.2018.08.034.
[20] Hu YN, Wu SC, Wu ZK, Zhong XL, Ahmed S, Karabal S, et al. A new approach to correlate the defect population with the fatigue life of selective laser melted Ti-6Al-4V alloy. Int J Fatigue 2020;136:105584. https://doi.org/10.1016/j.ijfatigue.2020.105584.
[21] Benedetti M, Santus C. Building the Kitagawa-Takahashi diagram of flawed materials and components using an optimized V-notched cylindrical specimen. Eng Fract Mech 2020;224:106810. https://doi.org/10.1016/j.engfracmech.2019.106810.
[22] Murakami Y, Takagi T, Wada K, Matsunaga H. Essential structure of S-N curve: Prediction of fatigue life and fatigue limit of defective materials and nature of scatter. Int J Fatigue 2021;146:106138. https://doi.org/10.1016/j.ijfatigue.2020.106138.
[23] El Haddad MH, Smith KN, Topper TH. Fatigue crack propagation of short cracks. J Eng Mater Technol 1979;101:42. https://doi.org/10.1115/1.3443647.
[24] El Haddad MH, Topper TH, Smith KN. Prediction of non propagating cracks. Eng Fract Mech 1979;11:573–84. https://doi.org/10.1016/0013-7944(79)90081-X.
[25] Murakami Y. Metal fatigue : effects of small defects and nonmetallic inclusions. II edition. Elsevier; 2019.

[26] INTERNATIONAL STANDARD ISO 4287:1997. Geometrical product specifications (GPS). Surface texture: profile method. Terms, definitions and surface texture parameters.
[27] INTERNATIONAL STANDARD ISO 25178-2:2022. Geometrical Product Specifications (GPS) – Surface Texture: Areal.
[28] Greitemeier D, Dalle Donne C, Syassen F, Eufinger J, Melz T. Effect of surface roughness on fatigue performance of additive manufactured Ti–6Al–4V. Mater Sci Technol 2016;32:629–34. https://doi.org/10.1179/1743284715Y.0000000053.
[29] Zhang J, Fatemi A. Surface roughness effect on multiaxial fatigue behavior of additive manufactured metals and its modeling. Theor Appl Fract Mech 2019;103:102260. https://doi.org/10.1016/j.tafmec.2019.102260.
[30] Nakatani M, Masuo H, Tanaka Y, Murakami Y. Effect of surface roughness on fatigue strength of Ti-6Al-4V alloy manufactured by additive manufacturing. Procedia Struct Integr 2019;19:294–301. https://doi.org/10.1016/j.prostr.2019.12.032.
[31] Barricelli L, Beretta S. Analysis of prospective SIF and shielding effect for cylindrical rough surfaces obtained by L-PBF. Eng Fract Mech 2021;256:107983. https://doi.org/10.1016/j.engfracmech.2021.107983.
[32] Schneller W, Leitner M, Pomberger S, Grün F, Leuders S, Pfeifer T, et al. Fatigue strength assessment of additively manufactured metallic structures considering bulk and surface layer characteristics. Addit Manuf 2021;40:101930. https://doi.org/10.1016/j.addma.2021.101930.
[33] Lee S, Rasoolian B, Silva DF, Pegues JW, Shamsaei N. Surface roughness parameter and modeling for fatigue behavior of additive manufactured parts: a non-destructive data-driven approach. Addit Manuf 2021;46:102094. https://doi.org/10.1016/j.addma.2021.102094.
[34] Gockel J, Sheridan L, Koerper B, Whip B. The influence of additive manufacturing processing parameters on surface roughness and fatigue life. Int J Fatigue 2019;124:380–8. https://doi.org/10.1016/j.ijfatigue.2019.03.025.
[35] Beretta S. More than 25 years of extreme value statistics for defects: Fundamentals, historical developments, recent applications. Int J Fatigue 2021;151:106407. https://doi.org/10.1016/j.ijfatigue.2021.106407.
[36] Fox JC, Pintar AL. Prediction of extreme value areal parameters in laser powder bed fusion of nickel superalloy 625. Surf Topogr Metrol Prop 2021;9:025033. https://doi.org/10.1088/2051-672X/AC0061.
[37] du Plessis A, Beretta S. Killer notches: The effect of as-built surface roughness on fatigue failure in AlSi10Mg produced by laser powder bed fusion. Addit Manuf 2020;35:101424. https://doi.org/10.1016/j.addma.2020.101424.
[38] Thompson A, Maskery I, Leach RK. X-ray computed tomography for additive manufacturing: a review. Meas Sci Technol 2016:27. https://doi.org/10.1088/0957-0233/27/7/072001.
[39] Diaz A. Surface texture characterization and optimization of metal additive manufacturing-produced components for aerospace applications. Addit Manuf Aerosp Ind, Elsevier 2019:341–74. https://doi.org/10.1016/B978-0-12-814062-8.00018-2.
[40] Downing D, Rogers J, Tino R, Elambasseril J, Wallbrink C, Qian M, et al. A virtual stylus method for non-destructive roughness profile measurement of additive manufactured lattice structures. Int J Adv Manuf Technol 2023;125:3723–42. https://doi.org/10.1007/s00170-023-10865-9.
[41] Atzori B, Lazzarin P. Notch sensitivity and defect sensitivity under fatigue loading: two sides of the same medal. Int J Fract 2000;107:L3–8.
[42] Atzori B, Lazzarin P, Meneghetti G. Fracture mechanics and notch sensitivity. Fatigue Fract Eng Mater Struct 2003;26:257–67. https://doi.org/10.1046/j.1460-2695.2003.00633.x.
[43] Atzori B, Lazzarin P, Meneghetti G. A unified treatment of the mode I fatigue limit of components containing notches or defects. Int J Fract 2005;133:61–87. https://doi.org/10.1007/s10704-005-2183-0.
[44] Rigon D, Meneghetti G. An engineering estimation of fatigue thresholds from a microstructural size and Vickers hardness: application to wrought and additively manufactured metals. Int J Fatigue 2020;139:105796. https://doi.org/10.1016/j.ijfatigue.2020.105796.
[45] Rigon D, Meneghetti G. Engineering estimation of the fatigue limit of wrought and defective additively manufactured metals for different load ratios. Int J Fatigue 2022;154:106530. https://doi.org/10.1016/j.ijfatigue.2021.106530.
[46] Kitagawa H, Takahashi S. Applicability of fracture mechanics to very small cracks or the cracks in the early stage. Proc 2nd int conf mech Behav Mater - 1976; ICM2:627–31.
[47] Yang ZG, Zhang JM, Li SX, Li GY, Wang QY, Hui WJ, et al. On the critical inclusion size of high strength steels under ultra-high cycle fatigue. Mater Sci Eng A 2006;427:167–74. https://doi.org/10.1016/j.msea.2006.04.068.
[48] Schönbauer BM, Mayer H. Effect of small defects on the fatigue strength of martensitic stainless steels. Int J Fatigue 2019;127:362–75. https://doi.org/10.1016/j.ijfatigue.2019.06.021.
[49] Chapetti MD. A simple model to predict the very high cycle fatigue resistance of steels. Int J Fatigue 2011;33:833–41. https://doi.org/10.1016/j.ijfatigue.2010.12.010.
[50] DuQuesnay DL, Yu MT, Topper TH. An analysis of notch size effect on the fatigue limit. J Test Eval 1988;4:375–85.
[51] Yu MT, DuQuesnay DL, Topper TH. Notch fatigue behaviour of SAE 1045 steel. Int J Fatigue 1988;10:109–16.
[52] Newman J, Raju I. Stress-intensity factor equations for cracks in three-dimensional finite bodies. Fract Mech Fourteenth Symp -Volume I Theory Anal 1983.
[53] Romano S, Brückner-Foit A, Brandão A, Gumpinger J, Ghidini T, Beretta S. Fatigue properties of AlSi10Mg obtained by additive manufacturing: Defect-based modelling and prediction of fatigue strength. Eng Fract Mech 2018;187:165–89. https://doi.org/10.1016/j.engfracmech.2017.11.002.
[54] Romano S, Nezhadfar PD, Shamsaei N, Seifi M, Beretta S. High cycle fatigue behavior and life prediction for additively manufactured 17–4 PH stainless steel: effect of sub-surface porosity and surface roughness. Theor Appl Fract Mech 2020;106:102477. https://doi.org/10.1016/j.tafmec.2020.102477.
[55] Molaei R, Fatemi A, Sanaei N, Pegues J, Shamsaei N, Shao S, et al. Fatigue of additive manufactured Ti-6Al-4V, Part II: The relationship between microstructure, material cyclic properties, and component performance. Int J Fatigue 2020;132:105363. https://doi.org/10.1016/J.IJFATIGUE.2019.105363.
[56] Gumbel EJ. Statistics of Extremes. Columbia University Press; 1958.
[57] Beretta S, Murakami Y. statistical analysis of defects for fatigue strength prediction and quality control of materials. Fatigue Fract Eng Mater Struct 1998;21:1049–65. https://doi.org/10.1046/J.1460-2695.1998.00104.X.
[58] ASTM E2283-08: Standard Practice for Extreme Value Analysis of Nonmetallic Inclusions in Steel; 2015. https://doi.org/10.1520/E2283-08R19.
[59] Beretta S, Murakami Y. Largest-extreme-value distribution analysis of multiple inclusion types in determining steel cleanliness. Metall Mater Trans B 2001.517–23.;2001(323):32. https://doi.org/10.1007/S11663-001-0036-4.
[60] INTERNATIONAL STANDARD ISO 6507. Metallic materials — Vickers hardness test fourth edition 2018.
[61] INTERNATIONAL STANDARD ISO 4288:1998. Geometrical Product Specifications (GPS) - Surface texture: Profile method - Rules and procedures for the assessment of surface texture.
[62] ISO 16610-61:2015+A1:2020 Geometrical product specification (GPS) – Filtration.
[63] Seewig J, Scott PJ, Eifler M, Barwick B, Hüser D. Crossing-The-line segmentation as a basis for Rsm and Rc evaluation. Surf Topogr Metrol Prop 2020;8:024010. https://doi.org/10.1088/2051-672X/AB958C.
[64] International Standard ISO 12107:2003. Metallic materials — Fatigue testing — Statistical planning and analysis of data.
[65] International Standard ISO 6892:2016. Metallic materials — Tensile testing — Part 1: Method of test at room temperature.
[66] Hamidi Nasab M, Romano S, Gastaldi D, Beretta S, Vedani M. Combined effect of surface anomalies and volumetric defects on fatigue assessment of AlSi7Mg fabricated via laser powder bed fusion. Addit Manuf 2020;34:100918. https://doi.org/10.1016/j.addma.2019.100918.
[67] Sausto F, Romano S, Patriarca L, Miccoli S, Beretta S. Benchmark of a probabilistic fatigue software based on machined and as-built components manufactured in AlSi10Mg by L-PBF. Int J Fatigue 2022;165:107171. https://doi.org/10.1016/j.ijfatigue.2022.107171.
[68] Murakami Y. Inclusion rating by statistics of extreme values and its application to fatigue strength prediction and quality control of materials. J Res Inst Stand Technol 1994;99:345–51.
[69] Evans MJ, Rosenthal JS. Probability and statistics: The science of uncertainty. 2nd ed. Macmillan; 2004.
[70] Barricelli L, Patriarca L, du Plessis A, Beretta S. Orientation-dependent fatigue assessment of Ti6Al4V manufactured by L-PBF: Size of surface features and shielding effect. Int J Fatigue 2023;168:107401. https://doi.org/10.1016/J.IJFATIGUE.2022.107401.